

# **Final Report**

**Airborne Aero-Optical Laboratory - Transonic  
N00014-16-1-3186**

**Eric J. Jumper  
Professor, University of Notre Dame  
Department of Aerospace and Mechanical Engineering  
University of Notre Dame  
Notre Dame, IN 46556**

**29 November, 2018**

## **Abstract**

This report covers the first and second year of this ONR grant, but it is the fourth and fifth years of the Airborne Aero-Optics Laboratory-Transonic (AAOL-T) program, whose first three years were under an AFOSR grant. Aero-optics severely limits an airborne directed-energy system's lethal field of regard; aero-optics refers to the deleterious effect that the density fluctuations in the flow have on an airborne optical system. The AAOL-T program studies aero-optical aberration problems from experimental, theoretical and computational approaches; the most unique part of the program is that we also perform flight tests using Falcon 10's, capable of testing at greater than Mach 0.8. The program makes use of two aircraft, one to project a small-aperture, diverging beam toward an optical turret on the second, laboratory aircraft. The fourth and fifth years of the program have been productive with flights in support of both the baseline program and to support AFRL/DARPA 40% ABC Turret testing. During the baseline program, extensive measurements of aero-optical environment around both hemisphere-on-cylinder and hemisphere-only turrets were performed for Mach range between 0.5 and 0.8.

# **Airborne Aero-Optics Laboratory – Transonic (AAOL-T)**

## **I. INTRODUCTION**

This report covers the final two years of an original 5-year HEL-JTO Grant that began its first three years as an AFOSR Grant, FA9550-13-1-0001 which ended in 2015. Because of administrative problems, the last two years of the Grant became administered by ONR under ONR / DE-JTO Grant N00014-18-1-2112, whose performance period ended in August 2018. The final report from the AFOSR Grant is attached as an appendix. This report covers the period from August 2016 to August 2018. As the title implied, the primary research in AAOL-T covers the collection and analysis of aero-optics. In its most restrictive definition, aero-optics refers to the deleterious effect that the density fluctuations in the flow over the exit or receiving pupil have on an airborne optical system, thus the name “aero-optics.” Except for some wavefront gathering on the AirBorne Laser, ABL, near the end of its program to assess aero-optic scaling laws, the AAOL [1] and present AAOL-T programs are the only programs to collect high-quality, aero-optically-aberrated wavefront data in flight [2,3,4]. The AAOL-T program continues to include Aero-Optics, the focus of AAOL, as its primary focus but at higher Mach numbers [5]; however, the AAOL-T program has additional objectives that were not part of AAOL: these specifically include aero-mechanical studies (i.e., aero-buffet of the turret and induced jitter), more emphasis on mitigation approaches that include adaptive optics, and specific emphasis on support of other programs.

The laboratory Falcon 10 is owned by Notre Dame, N100ND, and was donated to the program by Mr. Matthew McDevitt. At least in the near term, a video of the Notre Dame open house for the AAOL-T can be viewed at: <http://news.nd.edu/news/49299-falcon-10-aircraft-donation-enables-research-at-transonic-speeds/>. The program uses two Falcon 10's, the donated Falcon and a second Falcon which prior to the ONR Grant was rented from Northern Jet Management; however, due to some FAA changes, Notre Dame ended up purchasing the second Falcon 10, N349JC, so that Notre Dame now owns and maintains both aircraft. It should not be forgotten that the program also includes computational work and testing in wind tunnels.

## **II. AAOL-T FLIGHT-TESTS**

In a standard data-acquisition flight test, two Falcon 10s fly in formation at a nominal 50 m separation as shown in Figure 1. A diverging small-aperture 0.532  $\mu\text{m}$  laser is directed from the source aircraft to the turret on the laboratory aircraft, diverging to over fill the turret aperture.



**Figure 1. Formation flight with nominal 50 m separation showing diverging source beam emanating from the source aircraft and overfilling turret aperture on laboratory aircraft**



**Figure 2. View from inside the source aircraft.**

The baseline AAOL turret can be configured as either a hemisphere, a hemisphere with a cylindrical base, a spherically-conformal window, a flat window and some geometry changes at the base of the turret. All of these configurations were flown in the previous program at Mach numbers less than Mach 0.7 and these have all been re-flown at Mach Numbers up to Mach 0.8. In addition, the AAOL-T program supported testing of the Air Force Research Laboratory (AFRL/RD/DARPA) 40% ABC Turret. Figure 3 shows a typical setup for an AAOL-T flight experiment. The upper right hand corner of the figure shows from right to left the optical box to which the turret extends out of a newly-built door, designed to allow the turret to extend into the slip stream and form a pressure seal. Above the optical box is the turret control computer. The beam from the incoming laser from the chase plane is projected onto the optical bench to the fine track PDS and FSM systems and then to the various instruments. In the lower right corner of Figure 3 there is a schematic shown a setup used to gather wavefronts, usually at a frame rate of from 30 – 50 kHz with subaperture resolutions from 33X33 to 64X64.





- **Two aircraft in close formation**
  - **50m separation**
- **Source aircraft projects diverging beam onto laboratory aircraft**
- **Acquire high speed wavefronts**
  - **Simultaneous flight parameter acquisition**

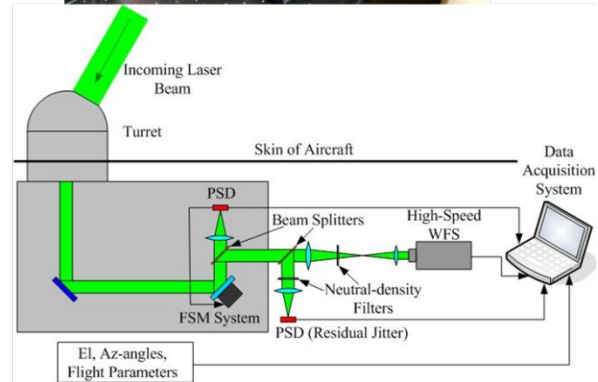


**Figure 3. Typical AAOL-T Flight Experiment Setup.**

The Flight Campaigns starting with the August 2015 ABC 40% Turret Support Through the August 2018 Campaign are listed in Table 1. It should be noted that these campaigns which will be describe in more detail later, cover research from basic to applied, the applied being covered under the objective to support other efforts for DoD research.

As shown in Figure 4a, this supports our original mission statement for the original AAOL and this AAOL-T program of developing a process to take concepts from ideas to relevant TRL levels that can find their way onto systems. This is demonstrated in Figure 4b explaining the TRL levels. Notice under the Analysis/Simulation column our program raises the TRL level to 6 (wind tunnel) to 7 (flight) and in some cases as in the ONR/NAVAIR support (Table 1, item VI.) to level 8.

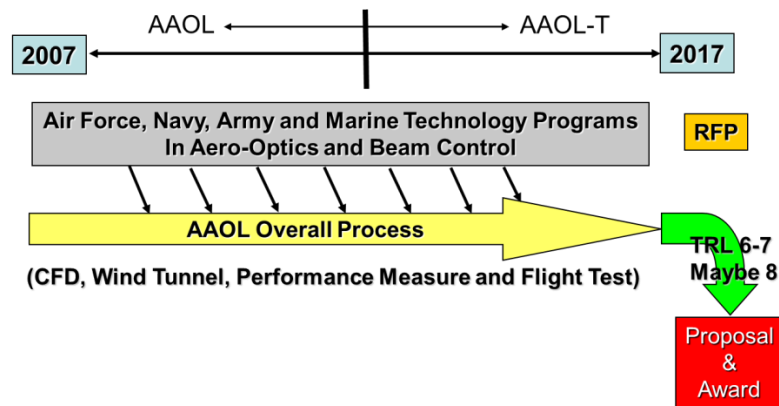


**Figure 4a. Original Mission Goal.**

## Technology Readiness Level (TRL) Descriptions Product, Process, Simulation

	TRL	Product	Process	Analysis/Simulation
<b>Implementation</b>	<b>9</b>	Actual System "Flight Proven" Through Successful Mission Ops.	Actual Process Proven Through Successful Operation by Program	Actual Models In Use By The Community
<b>Validation/ Verification</b>	<b>8</b>	Actual System "Flight Qualified" Through Test & Demo	Actual Process Completed and "Qualified" Through Test/Demo	Actual Models are validated against "Flight Qualified" data
	<b>7</b>	System Prototype Demonstration In an Operating Environment	Prototype Process Demo In a Program Environment	Prototype Model Validated Against Flight-Test Data
<b>Demonstration</b>	<b>6</b>	System/ Subsystem Prototype Demo In a Relevant Environment	Process Prototype Demo In a Relevant Environment	Model Validated Against Relevant Ground-Test Data
	<b>5</b>	Component Validation In Relevant Environment	Beta Version Key Elements Validated In Relevant Env.	Model Components Evaluated Against Relevant Data
<b>Development</b>	<b>4</b>	Component Validation In Laboratory Environment	Alpha Version Key Elements Validated Against Benchmark	Tools Assembled Into Package and Tested Against Hand Calcs.
<b>Proving Feasibility</b>	<b>3</b>	Critical Function of Characteristic Proof-of-Concept.	Alpha Version Operational In a Test Environment	Data Flow Diagrams, Tools Collection and Familiarization
<b>Basic Research</b>	<b>2</b>	Technology Concept and/or Application Formulated	Requirements Document Approved By Customer	Methods and Algorithms for Similar Systems Identified
	<b>1</b>	Basic Principles Observed and Reported	Current Process Documents and Potential Savings Identified	System Characterized and Tool Needs Defined

**Figure 4b. Description of TRL levels.**

**TABLE 1**

### AAOL-T Flight Campaigns

- I. ABC 40% Turret**
  - 9 Sorties, August 26 – 31, 2015
- II. HEL JTO MRI/ ABC Support Campaign 7**
  - 7 Sorties February 22 – 28, 2016
- III. ABC Support Campaign 8**
- IV. HEL JTO MRI Boundary-Layer Study**
  - 3 Sorties March 29 – 30, 2016
- V. HEL JTO MRI Global Fence**
  - 6 Sorties April 26 – May 2, 2016
- VI. ONR / NAVAIR**
  - 4 Sorties June 26 – 29, 2016
- VII. HEL JTO MRI Imaging**
  - 4 Sorties Sept 9 – 10, 2016
- VIII. Mitigation Study**
  - 4 Sorties Oct 16 – 21, 2016
- IX. HEL JTO MRI**
  - 4 Sorties Oct 17 – 20, 2016
  - Imaging Study
- X. HEL JTO MRI Imaging**
  - 4 sorties May 9 – 10 , 2017

### III. RESEARCH ASSOCIATED WITH FLIGHT EXPERIMENTS

It should be noted that results from our support efforts for ONR/NAVAIR and AFRL/DARPA along with some of the MRI work that later was determined to have limited access are not included in this report. Rather, in this section the research performed that has unlimited access will be described.

**Wavefront Contamination by Acoustic Disturbances.** While analyzing wavefront data from the March 2016 Campaign, Dr. D.J. Whittich, AFRL/RD, noticed some periodic structures in wavefronts for  $Az = 87^\circ$ ,  $El = 37^\circ$  at Mach 0.5 in wavefronts that were expected to be very quiet in the sense that it represented propagation through an attached turbulent boundary layer. Furthermore, such structures were not representative of years of wavefront data taken for propagation through attached turbulent boundary layers. Our initial reaction was to assume that

these wavefront structures must be due to noise, i.e., contamination, or mechanical vibrations. Figure 5 is one wavefront frame from the campaign. The wavefront is from a turret viewing angle of angle of  $Az = 87^\circ$ ,  $El = 37^\circ$  where  $0.0^\circ$   $Az$  is looking directly into the oncoming flow. At these angles the flow is fully attached to the lens over the aperture. The flow is from left to right. Analysis of the time series from which the wavefront was taken showed that the disturbance was moving upstream into the oncoming flow. Computation of the  $OPD_{rms}$

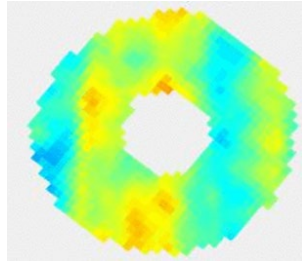


**Figure 5. Wavefront showing the vertical stripes.**

showed that while the  $OPD$  was small, it was a bit larger than it should be. Interestingly as the  $Az$  was slewed off  $\sim 87^\circ \pm 5^\circ$ , the  $OPD$  dropped down to expected level and the stripes no longer appeared in the wavefronts.

The time series of wavefronts were then analyzed using Proper Orthogonal Decomposition (POD). This is done by decomposing the wavefront series into its fundamental spatial modes as

$$OPD(x, y, t) = \sum_n a_n(t) \phi_n(x, y)$$

Where  $\phi_n(x,y)$  are the POD modes and  $a_n(t)$  are the temporal eigenvalues. The POD modes are computed using

$$\int R(x,y;x',y')\phi_n(x',y')dx'dy' = \lambda_n\phi_n(x,y)$$

$$R(x,y;x',y') = \overline{OPD(x,y,t)OPD(x',y',t)}$$

$$\lambda_n = \overline{a_n^2(t)}$$

This allowed us to examine the spectra of the temporal eigenvalues for specific modes and reconstruct a time series of using only those specific modes. Further we could examine the relative mode energy of the selected modes at different turret angles. The stripe characteristics were found to be present primarily in Modes 2, 3 and 4. These Modes are shown in Figure 6.

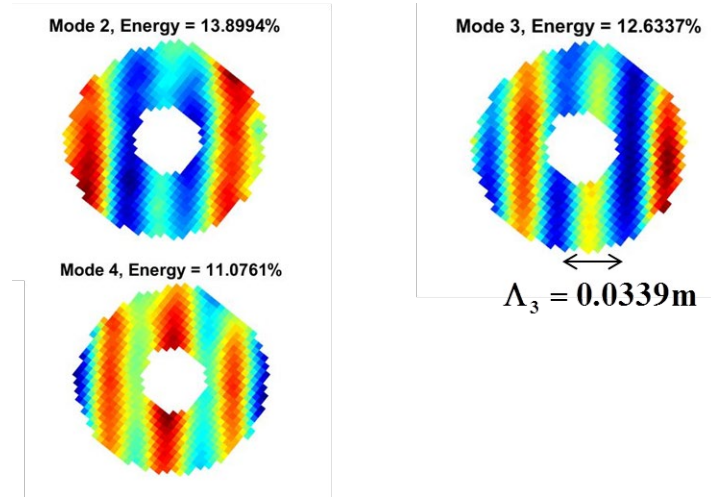


**Figure 6. Spatial POD Modes for Modes 2,3 and 4 also showing the energy contained in those modes as a percent of energy in all modes and the typical structure size in Mode 3 in actual space**

It can be seen that these three modes contain  $\sim 40\%$  of the total wavefront distortion energy. The eigenvalue for  $a_3(t)$  is shown in Figure 7 along with its spectra. Notice that the frequency peaks at 4.717 kHz. Similar analysis performed at only a few degrees off still showed similar modes with similar frequencies, but at much lower mode energy, eventually dropping to 3% and less of the total wavefront energy by  $5^\circ$  off angle dropping off to nearly 0% by  $10^\circ$ .

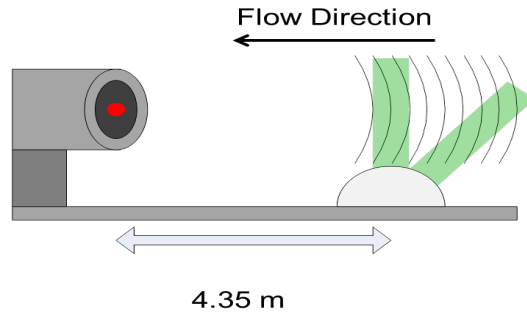


**Figure 7. Geometry of engine and turret**

All these characteristics suggested that the wavefronts were imprinting acoustic disturbances from the turbofan engine whose inlet was 4.35 m downstream from the turret centerline. Figure 7 shows the geometric association of the turret location with the turret along with the rationale for why the imprinting was only pronounced at  $\sim 90^\circ$ . When off angle the waves would tend to cancel.

The waves would propagate at the speed of sound into the incoming flow so that the waves convective speed would be

$$U_c \cong c - U_\infty$$

where  $U_c$  is the convective velocity,  $c$  is the speed of sound and  $U_\infty$  is the incoming flow speed. Given the OPD of the wavefronts it was possible to estimate the engines sound pressure level, SPL. Referring to Figure 8, the OPD was obtained by integrating through the acoustic disturbance some length  $L$ . Based on the fall off of energy determined from different slew angles,  $L$  was estimated to be  $\sim 0.4$  m; then the SPL was estimated to be  $\sim 115$  dB, as follows:

$$\begin{aligned} \text{SPL} &= 20 \log_{10} \frac{P_{\text{RMS}}}{P_{\text{ref}}} \rightarrow P_{\text{RMS}} = P_{\text{ref}} 10^{\frac{\text{SPL}}{20}}, P_{\text{ref}} = 20 \mu\text{Pa} \\ \text{OPD}_{\text{RMS}} &\approx K_{\text{GD}} \int_0^L \rho_{\text{RMS}} dl \approx K_{\text{GD}} \rho_{\text{RMS}} L \\ \rho_{\text{RMS}} &= \frac{P_{\text{RMS}}}{\gamma RT} \\ \text{OPD}_{\text{RMS}} &\approx \frac{K_{\text{GD}} L P_{\text{ref}}}{RT} 10^{\frac{\text{SPL}}{20}} \\ \text{OPD}_{\text{RMS}} &= 0.02 \mu \rightarrow \text{SPL} \approx 115 \end{aligned}$$

Based on SPL measurements on the ground, 115 dB was a reasonable SPL [6].

**Wind-Tunnel Boundary-Layer Study.** From a basic research point of view, large scale structures in a turbulent boundary layer have long been of research interest [See Ref 7, for example]. Large scale structures are also the most optically active. Adaptive-Optic systems can be tuned to correct distortions caused by large scale structures [8]. Once the large scale structures have been studied, their convective nature can be leveraged to develop latency tolerant Adaptive-Optic controllers. Further, wavefront sensors now offer a way to study these structures that has not been available with other instruments.

A wind-tunnel experiment was performed with an experimental set up shown in Fig. 8. It shows a double-pass through two boundary layers, one on each side of the Notre Dame Trisonic Wind Tunnel facility. At the interrogation point the Reynolds number based on the boundary layers' momentum thicknesses was  $Re_\theta = 15,500$ , Reynolds number based on skin-friction velocity,  $Re_\tau = 4,780$  and the Mach number was 0.5 and the boundary layer thicknesses were  $\delta = 15.6$  mm. It should also be noted that the aperture is limited [9].

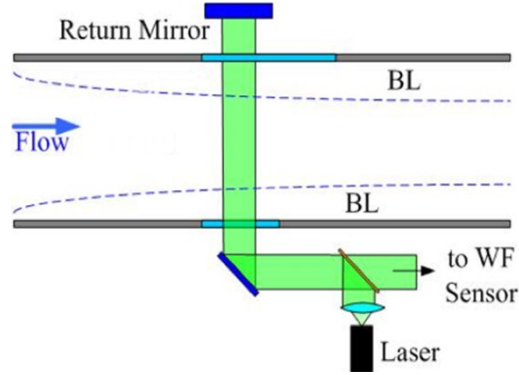


**Figure 8. Experimental setup for turbulent boundary-layer study**

A companion experiment was also performed at Caltech in their turbulent boundary-layer facility. In this experiment the structures could only be seen by slightly heating the flow upstream of the viewing port. Only one side was heated so although it was again double pass, only one boundary layer was interrogated. The boundary layers momentum thickness was  $Re_\theta = 2,100$ , Reynolds number based on skin-friction velocity,  $Re_\tau = 1,200$  and the Mach number was 0.03 and the boundary layer thicknesses were  $\delta = 35$  mm. The setup is shown in Figure 9, notice that in this experiment the aperture was again limited.

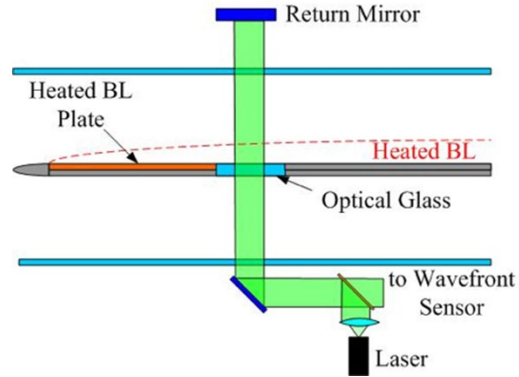


**Figure 9. Caltech Setup**

In both experiments full 2D wavefronts were collected with varying spatial and temporal resolution. The relevant information on all the experiments is given in Table 2 and the results from these experiments are shown in Fig. 10.

Table 2, Boundary Layer

Name	M	Subapertures	$Ap/\delta$	Sampling Frequency (Hz)
F04	0.5	46x46	3.88	49,000
F06	0.5	25x34	2.84	100,000
F12	0.5	21x22	3.02	130,000
C01	0.03	40x41	1.37	25,000



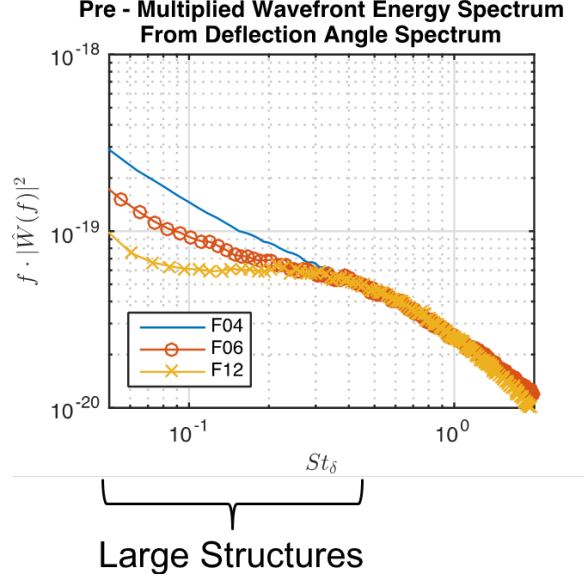


**Figure 10. Spectrum of Deflection Angles in the streamwise direction from the subapertures in the wavefront sensor data**

What is clear from Fig. 10 is that the high-frequency jitter due to the passing structures are all similar; however, the low-frequency, larger-structure spectra diverge based on aperture to boundary layer ratios shown in Table 2. The low-frequency spectra is lost since in processing the wavefronts the overall tip-tilt is removed, leaving only the higher-order aberration information for structures smaller than the aperture.

It is clear that this low frequency tip-tilt information is important because it is directly related to beam jitter which must be removed by a fast steering mirror, FSM. In this MRI, we researched how this information might be recovered from wavefronts that have apertures smaller than the largest aero-optic aberration through which the laser passes. This information is important to know independently because wavefronts collected either in the air or in wind tunnels also have overall tip-tilt imposed by vibration and buffet which is why the overall tilt is removed prior to processing the wavefronts. Our research was thus aimed at recovering only the aero-optic tilt.

A wavefront can be broken down into higher-order wavefront,  $w(x,y,t)$ , overall Tip-Tilt and piston (also removed in processing) as follows:

$$W(x, y, t) = w(x, y, t) + Ax + By + C$$

Furthermore, piston is an unknown quantity,  $(\theta_x, \theta_y) = -\nabla W$ . Although boundary-layer structures evolve, the evolution is slow compared to the convection so that they primarily convect. A longer than structure size can thus be well estimated by allowing them to convect and restoring piston and tip-tilt to preserve smooth wavefront surfaces. Time can then be traded for space to construct a long wavefront “strip” from a time series of wavefront data taken at sufficient frame rate to assure some overlap. Figure 11 shows two wavefront frames where the same structure is present in both frames, i.e., overlap.

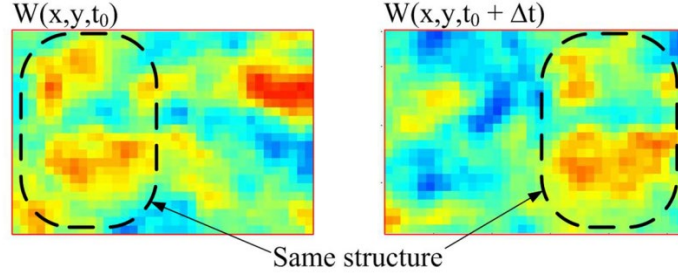


**Figure 11. Two “overlapping” wavefront frames**

In the overlapping region between frames the tip, tilt and piston is adjusted until a minimum in the RMS error is found.

$$A, B, C \leftarrow \min_{OR} \int (w_1 - \tilde{w}_2)^2 dOR$$

Once the frames have been tip, tilt, and piston corrected they can be averaged together to form the stitched wavefront. This process trades time for space and reveals large-scale structures that were not available in single aperture-restricted wavefronts, as shown in Fig. 12.

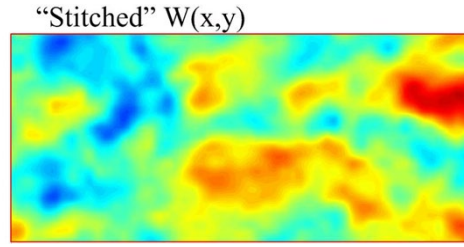


**Figure 12. Stitched Wavefront,  $W(x,y)$  from two in Fig. 11**

A longer stitched strip is shown in Fig. 13, also highlighted in the Fig. 11 and 12 wavefronts. As can be seen long structures are now fully captured in the strip. Frequency spectra now show energy in the low-frequency portion of the data, as shown in Fig. 14. Note that the peak energy for  $Ap/\delta$  of 3 and twenty are close indicating that the largest structures can be captured with  $Ap/\delta$  of from 3 – 5 [12].

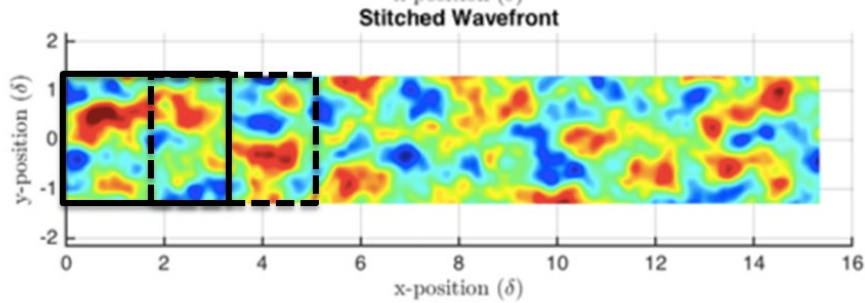


**Figure 13. Longer Strip wavefront shown the large-scale structures**

As shown in Fig. energy deficit and peak location shift can be attributed to tip/tilt removal



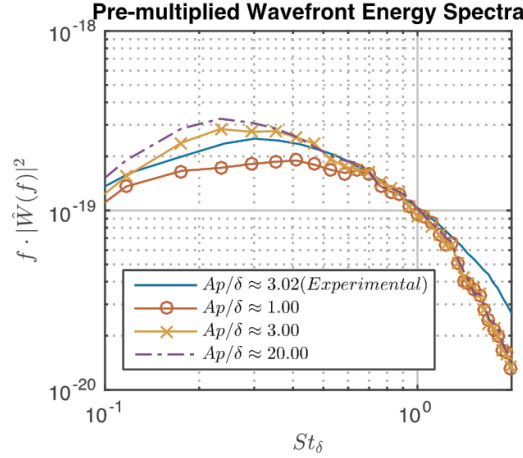


Figure 14. Spectra based on generated Strip from Fig. 13

**Imaging Experiments.** Toward the end of the Grant, we began performing imaging experiments using the Falcon 10 aircraft. These experiments were motivated by the fact that part of any engagement requires target identification. As shown in Fig. 15, the aero-optical aberrations will reduce the focus to below that of range through a vacuum, also shown.

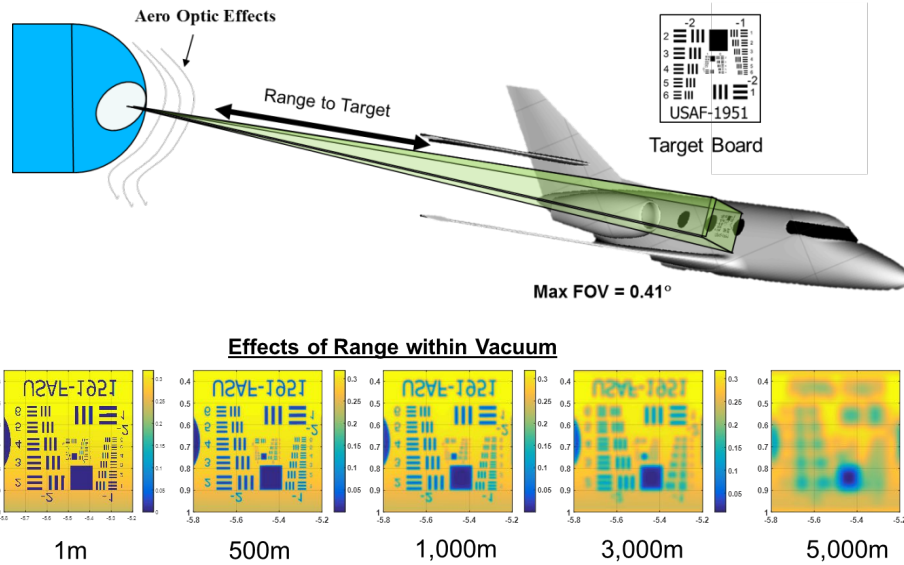
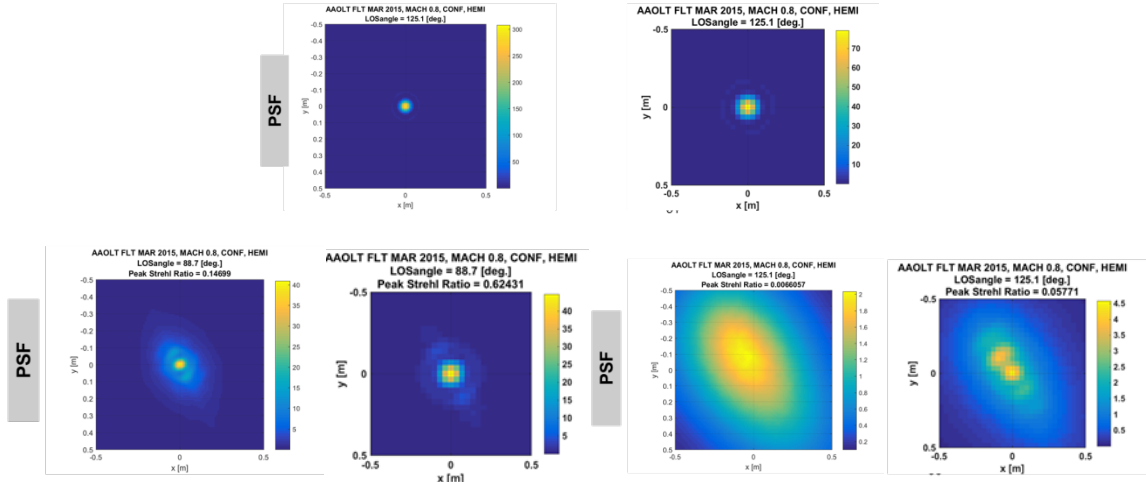


Figure 15. Effect of Aero-Optical on imaging

Based on collected aero-optics wavefronts collected it is possible to compare the Point Spread Function (PSF) for a vacuum, as shown in Fig. 16, with PSF based on flight data. Figure 16 shows the PSF for vacuum in the top at two ranges and the PSFs for a turret viewing angle of  $89^\circ$  at the same two ranges at lower left and at a view angle of  $125^\circ$  at the same two ranges in the lower right. At a viewing angle of  $89^\circ$  the aberration is due to an attached turbulent boundary layer which has low  $OPD_{rms}$ , but at  $125^\circ$  viewing angle the imaging is through a separated shear layer which has large  $OPD_{rms}$ .



**Figure 16. PSF for aero-optically-aberrated telescope, lower left through telescope at a viewing angle of 89°, lower right at a viewing angle of 125°, with that of a vacuum shown at the top**

The CONF and HEMI in the image indicates the turret configuration. This work was carried over into the follow-on DE-JTO MRI. The results from these and follow-on flight experiments are to be reported under the new grant.

**High-Fidelity Computations.** The high-fidelity computational work sponsored by the grant was initially performed to answer the question of “how good is good enough.” The goal was to use Computational Fluid Dynamics (CFD) to improve our understanding and predictive capability of turret aero-optics at realistic Reynolds and Mach numbers. This last provision is no minor requirement because our work was actually the highest Reynolds and Mach numbers computed using LES. The optical turret used on the AAOL was simulated using Wall-Modeled Large-Eddy Simulation (WMLES) at the actual flight Reynolds number of 2,300,000 and Mach number of 0.4. As it turned out, even the highest fidelity computations began to represent the flight data; however, even these did not fully validate using CFD to compute aero-optics. In the end we used Large-Eddy Simulation (LES) on more than 10,000 cores running for approximately one week. Even slight changes in turret geometry led to extensive modifications of the code; however, these computational studies were instructive in better understanding the flow field around a turret and how small geometric characteristics of a turret configuration can affect the aero-optics. Shown here are some of the highlights of this work. The results are being extensively reported in the literature and should be available within a few years.

The solver domain is shown in Fig. 17. The LES code used was the compressible CharLES code, developed at Cascade Technologies, Inc. It is a low-dissipative 2<sup>nd</sup> order finite volume code for spatial discretization. It is third-order Runge-Kutta in time. It uses a Vreman model for the subgrid-scale stress and an equilibrium stress-balanced wall model [13].

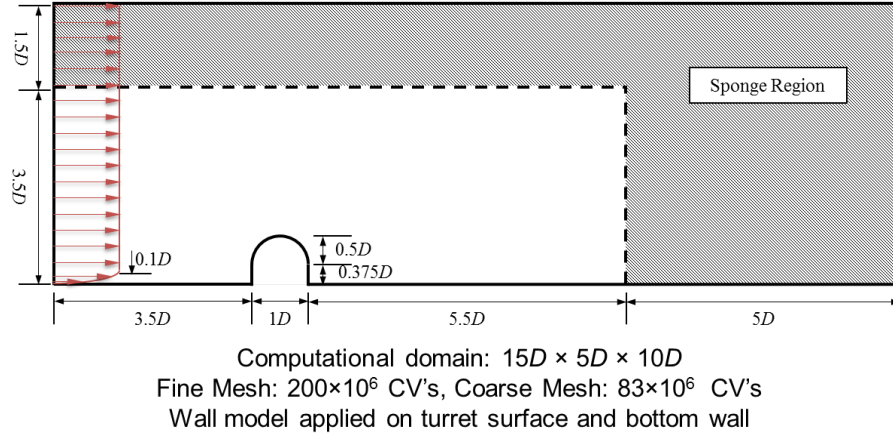


**Figure 17. Computational domain used for simulating Turret**

Figure 18 shows comparisons of the code results from separate measured flow parameters measured for the turret in our wind tunnel to validate the mesh insensitivity.

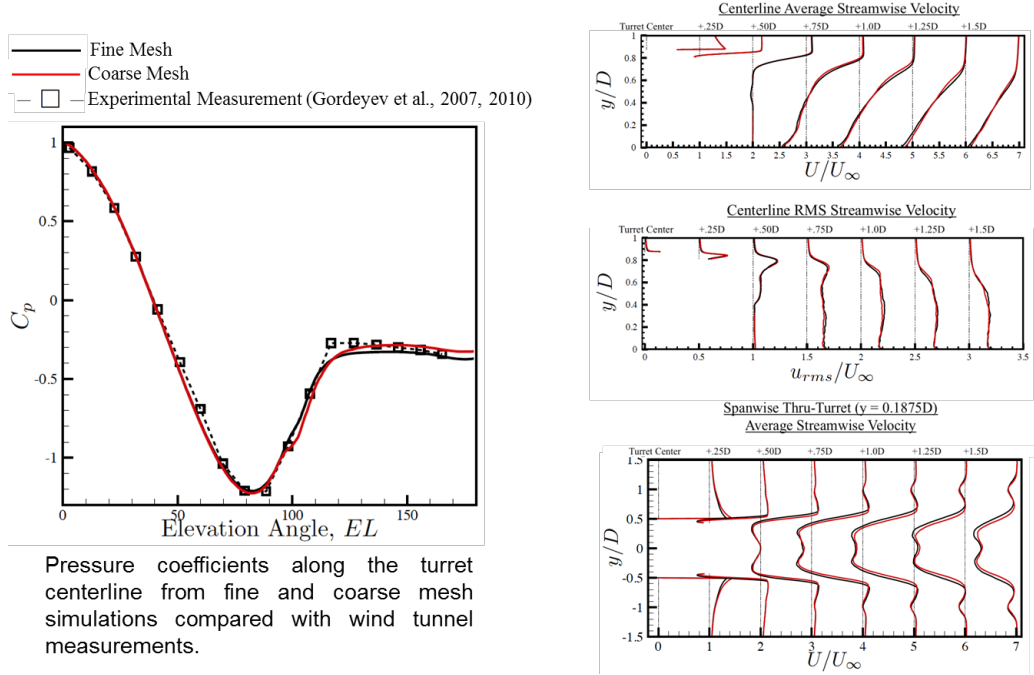


**Figure 18. Comparisons of code results with measured data to validate mesh independence**

Further results are shown in Figs. 19 -23. The mean surface streamlines are shown compared to oil-flow visualization in Fig. 19. Unsteady pressures were calculated and compared to experiments using pressure sensitive paint. Both computed unsteady pressure and experimental pressures were reduced to POD modes, as shown in Fig. 20. Several modes are common for experimental and computational results. In Fig. 21, compares  $OPD_{rms}$  along the centerline of the turret from simulations with different mesh grids compared to wind-tunnel experiments measuring  $OPD_{rms}$  using various sensors. Along the centerline the comparisons are the best we

have seen from any other type computations; however moving off centerline the  $OPD_{rms}$  amplitudes were under predicted from those of the experiments.

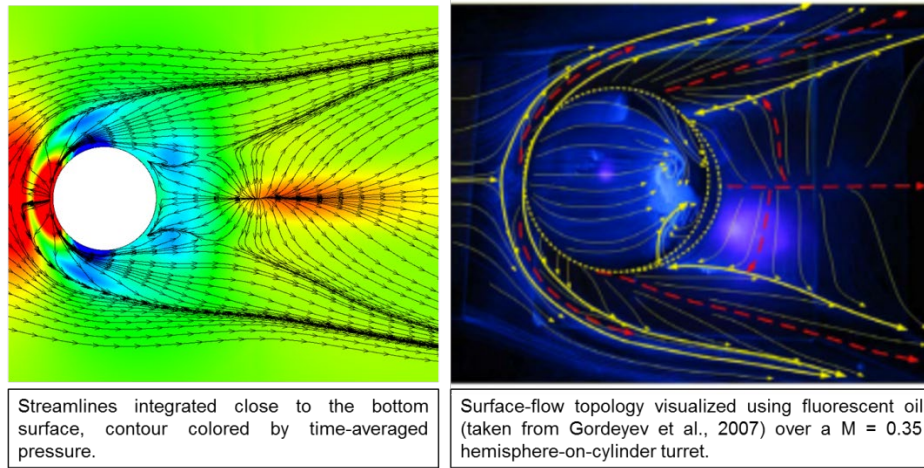


**Figure 19. Computed mean surface flow lines (left) compared to oil-flow visualization (right)**

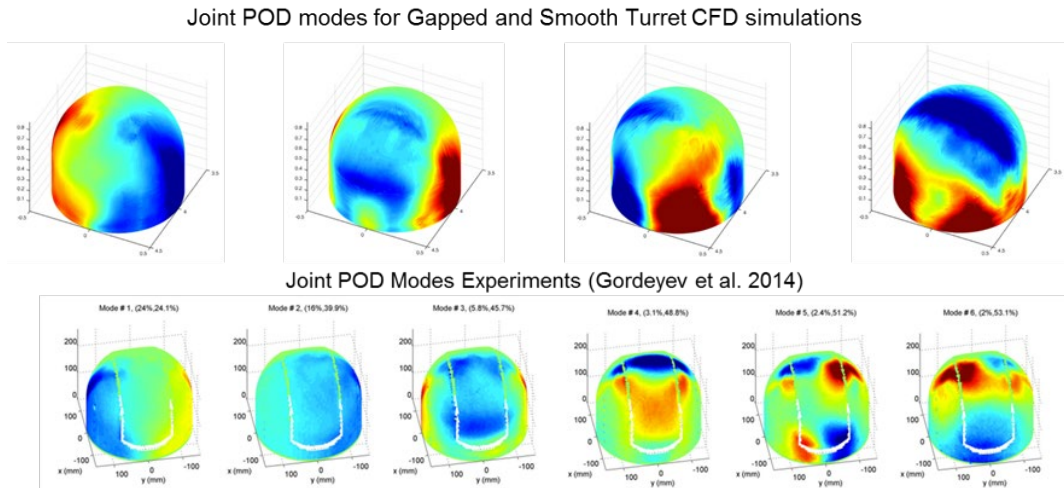


**Figure 20. Joint POD modes from simulations (top) and from experiment (bottom)**

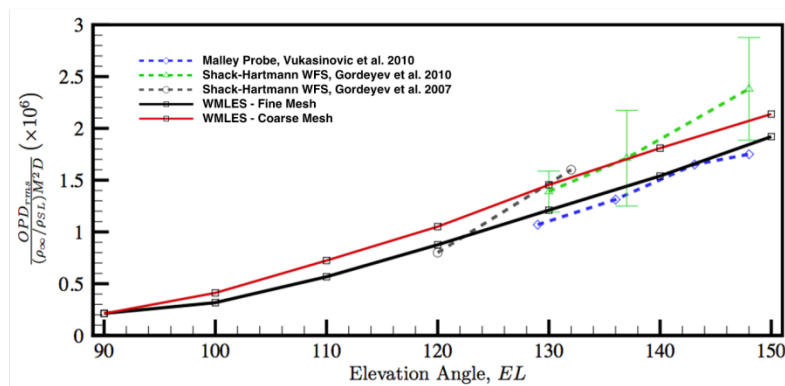


**Figure 21. Comparison of  $OPD_{rms}$  between computations and experiment**

One thing that is interesting about having a computed flow over a smooth turret is that it is possible to compute  $OPD_{rms}$  at any Az vs El position of interest. This was done for an  $Ap/D$  of 0.333 with the points indicating the center of the aperture. The locations and  $OPD_{rms}$  are shown in Fig. 22. The effect of the separation and horn vortex in the separated flow can be easily seen.

- **Optical data integrated and collected at 390 different angles**
  - Each time optics are calculated 5.4 million points per angle, 2.1 billion points in all are interpolated and integrated over
  - In total, ~3 TB of optical data was generated

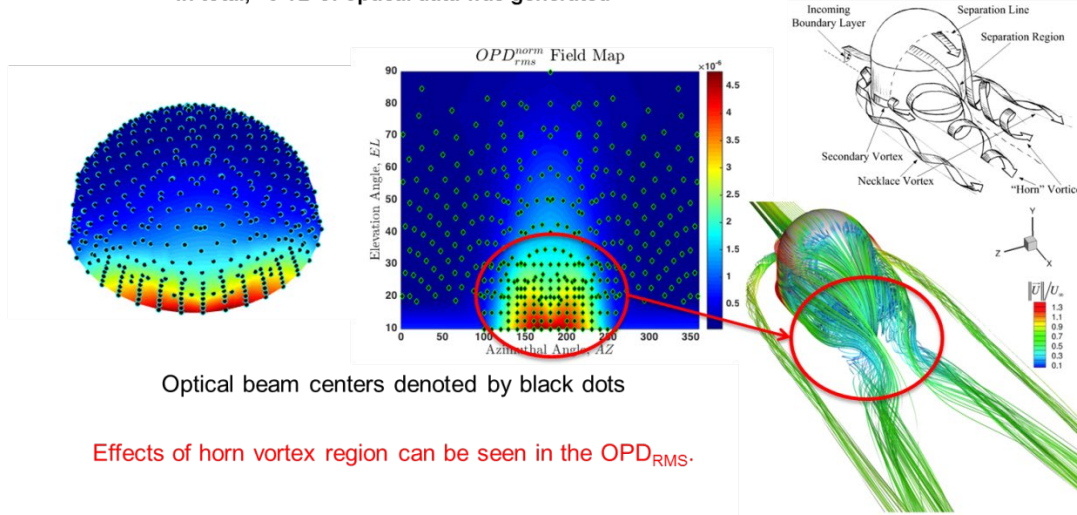


**Figure 21. Normalized  $OPD_{rms}$  vs Az and El position on turret.**

When these data are recast as normalized  $OPD_{rms}$  vs viewing angle a number of things jump out. First of all it is clear why the data diverges from a nice viewing/lookback angle,  $\alpha$ , curve shown in green with is universal over a fairly large range of modified elevation angle,  $\beta$ , as the aperture begins to encounter the horn vortices. It is in these regions that the computations under predict the amplitude of  $OPD_{rms}$ , whereas in the region where the curve collapses to the green curve the simulation does a fair job in matching experiment. While these were done for an  $Ap/D$  of 0.333, it was done for a number of aperture sizes to develop a relation as a function of aperture size.

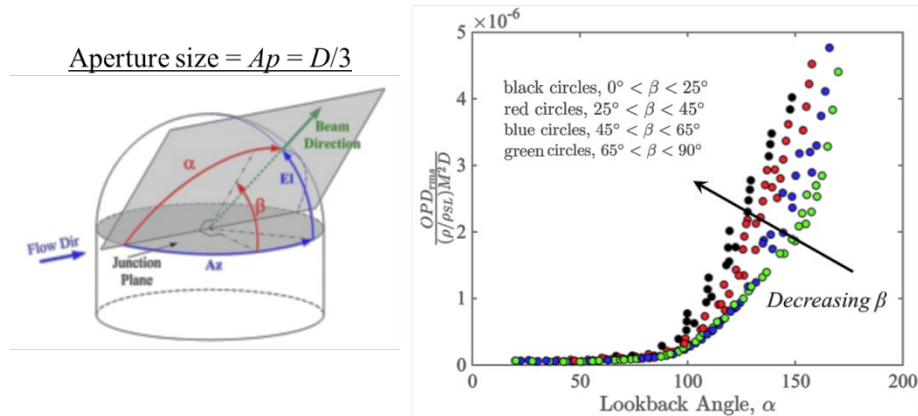


**Figure 22. Relationship for viewing angle,  $\alpha$ , and modified elevation angle,  $\beta$ , as a function of Az and El (left) and normalized viewing angle for  $\alpha$  and  $\beta$**



## References

- [1] E Jumper, M Zenk, S Gordeyev, D Cavalieri and M. Whiteley, "Airborne Aero-Optics Laboratory", Journal of Optical Engineering, 52(7), 071408, 2013.
- [2] C. Porter, S. Gordeyev, M. Zenk and E. Jumper, "Flight Measurements of the Aero-Optical Environment around a Flat-Windowed Turret", AIAA Journal, Vol. 51, No. 6, Jun. 2013, pp. 1394-1403.
- [3] N. De Lucca, S. Gordeyev and E.J. Jumper, "In-flight aero-optics of turrets", Journal of Optical Engineering, 52(7), 071405, 2013.
- [4] R. Burns, S. Gordeyev, E. Jumper, S. Gogineni, M. Paul and D.J. Wittich, "Estimation of Aero-Optical Wavefronts Using Optical and Non-Optical Measurements ", AIAA Paper 2014-0319, 2014.
- [5] A. Vorobiev, S. Gordeyev, E. Jumper, S. Gogineni, A. Marruffo and D.J. Wittich, "Low-Dimensional Dynamics and Modeling of Shock-Separation Interaction over Turrets at Transonic Speeds", AIAA Paper 2014-2357, 2014.
- [6] N. De Lucca, S. Gordeyev, E. Jumper and D.J. Wittich, " Effects of engine acoustic waves on optical environment around turrets in-flight on AAOL-T", Optical Engineering, 57(6), 064107, June 2018.
- [7] Dennis, D. J. C. and Nickels, T. B., "Experimental measurement of large-scale three-dimensional structures in a turbulent boundary layer. Part 1. Vortex packets," Journal of Fluid Mechanics, Vol. 673, 2011, pp. 180–217.
- [8] W.R. Burns, E.J. Jumper and S. Gordeyev, " A Latency-Tolerant Architecture for Airborne Adaptive Optic Systems ", AIAA Paper 2015-0679, 2015.
- [9] S. Gordeyev, A. E. Smith, J.A. Cress and E.J. Jumper, " Experimental studies of aero-optical properties of subsonic turbulent boundary layers", Journal of Fluid Mechanics, 740, pp. 214-253, 2014.
- [10] ] S. Gordeyev, J.A. Cress, A Smith and E.J. Jumper, " Aero-optical measurements in a subsonic, turbulent boundary layer with non-adiabatic walls", Physics of Fluids, 27, 045110, 2015.
- [11] S. Gordeyev, A.E. Smith, T Saxton-Fox and B. McKeon, " Studies of the large-scale structure in adiabatic and moderately-wall-heated subsonic boundary layers ", Paper 7A-3, 9th International Symposium on Turbulence and Shear Flow Phenomena (TSFP-9), 2015.
- [12] M.R. Kemnetz and S. Gordeyev, "Optical Investigation of Large-Scale Boundary-Layer Structures," AIAA Paper 2016-1460, 2016.
- [13] Mathews E., Wang K., Wang M., and Jumper E.J., "A Spectral Description of Aero-Optical Phase Distortions and the Effects of Turbulent Flow Scales," AIAA Aviation Meeting, 2017.

**Appendix A -- Final Report 2016**

**Airborne Aero-Optical Laboratory - Transonic  
FA9550-13-1-0001**

**Eric J. Jumper  
Professor, University of Notre Dame  
Department of Aerospace and Mechanical Engineering  
University of Notre Dame  
Notre Dame, IN 46556**

**3 October, 2016**

## **Abstract**

This report covers the third year of the Airborne Aero-Optics Laboratory-Transonic (AAOL-T) program. Aero-optics severely limits an airborne directed-energy system's lethal field of regard; aero-optics refers to the deleterious effect that the density fluctuations in the flow have on an airborne optical system. The AAOL-T program studies aero-optical aberration problems from experimental, theoretical and computational approaches; the most unique part of the program is that we also perform flight tests using Falcon 10's, capable of testing at greater than Mach 0.8. The program makes use of two aircraft, one to project a small-aperture, diverging beam toward an optical turret on the second, laboratory aircraft. The third year of the program has been productive with thirty-one flights flown in support of both the baseline program and to support AFRL/DARPA 40% ABC Turret testing, of which 5 flights plus seven at the end of September 2014 were under the baseline program. During the baseline program, extensive measurements of aero-optical environment around both hemisphere-on-cylinder and hemisphere-only turrets were performed for Mach range between 0.5 and 0.8. Fluidic environment was also studied in-flight by collecting simultaneous unsteady pressure data over an array of pressure sensors on the surface of these turrets for Mach between 0.5 and 0.8. In addition to collecting the aero-optical data in flight, the baseline data was used in a wide range of analysis of these data and using the data to explore advanced techniques in adaptive optics. The report describes mainly analysis of data and the computational work done in year three of the program.



# **Airborne Aero-Optics Laboratory-Transonic (AAOL-T) Progress Report**

## **I. INTRODUCTION**

This report covers the third year of the Airborne Aero-Optics Laboratory-Transonic (AAOL-T) Program. The partners in the program are Notre Dame, the Air Force Institute of Technology and MZA. Aero-optics severely limits an airborne directed-energy system's lethal field of regard; in its most restrictive definition, aero-optics refers to the deleterious effect that the density fluctuations in the flow over the exit or receiving pupil have on an airborne optical system, thus the name "aero-optics." Except for some wavefront gathering on the AirBorne Laser, ABL, near the end of its program to assess aero-optic scaling laws, the AAOL [1] and present AAOL-T programs are the only programs to collect high-quality, aero-optically-aberrated wavefront data in flight [2,3,4]. Both programs deal with aero effects on the optical beam control systems of airborne optical systems. Because AAOL-T is a continuation of AAOL many of the original objectives of the AAOL program are also part of the objectives of the present AAOL-T program. The AAOL-T program continues to include Aero-Optics as its primary focus but now at higher Mach numbers [5]; however, the new program has additional objectives that were not part of AAOL: these specifically include aero-mechanical studies, more emphasis on mitigation approaches that include adaptive optics, and specific emphasis on support of other programs. In the year-one annual report, we reported on approaches in understanding unsteady pressure data collected on the Cessna Citation version of the AAOL continued from the end of the AAOL program into the AAOL-T program. As will be described below, in our first safety-of-flight campaign using the new (Falcon 10) aircraft we flew the same pressure turret used in the Citation in conjunction with our first safety-of-flight campaign in February 2014. Also, our support of flight tests for the AFRL/DARPA 40% scale ABC turret began in year-two and is continuing as the report is being written.

Like the AAOL program, AAOL-T program makes use of two aircraft, one to project a small-aperture, diverging beam toward an optical turret on the second, laboratory aircraft. The title of the present grant ends with the word "Transonic;" and required that the program migrate from the Cessna Citation Bravos, which were limited to Mach ~0.7, to the Falcon 10 that can cruise above Mach 0.8. By February 2014, all of the modifications of the new Falcon 10 were complete and both baseline aero-optic data and unsteady pressure data have been taken and analyzed; our high-fidelity CFD effort has also continued. As in year two, this year has also been productive in producing journal articles and meeting papers.

The laboratory Falcon 10 is owned by Notre Dame and was donated to the program by Mr. Matthew McDevitt. At least in the near term, a video of the Notre Dame open house for the AAOL-T can be viewed at: <http://news.nd.edu/news/49299-falcon-10-aircraft-donation-enables-research-at-transonic-speeds/>.

## **II. AAOL-T FLIGHT-TESTS**

In a standard data-acquisition flight test, two Falcon 10s fly in formation at a nominal 50 m separation as shown in Figure 1. A diverging small-aperture 0.532  $\mu\text{m}$  laser is directed from the source aircraft to the turret on the laboratory aircraft, diverging to over fill the turret aperture.

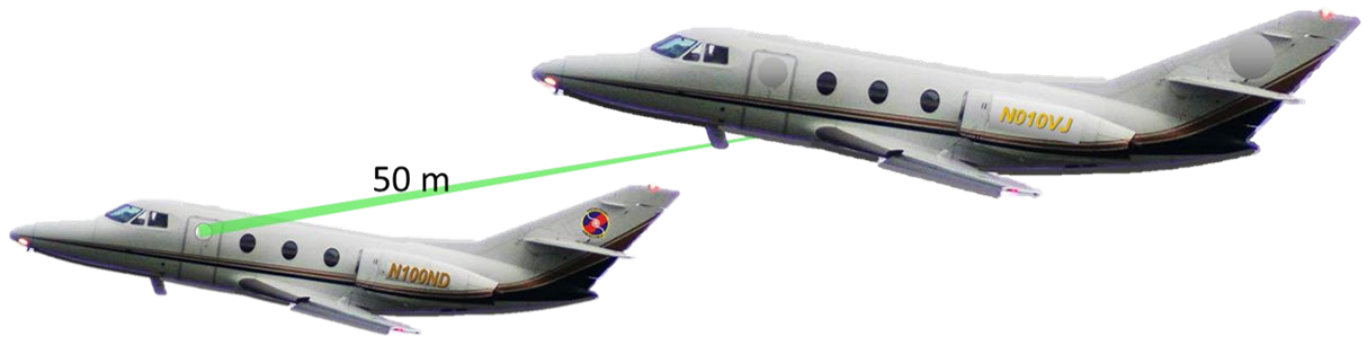


**Figure 1. Formation flight with nominal 50 m separation showing diverging source beam emanating from the source aircraft and overfilling turret aperture on laboratory aircraft**



**Figure 2. View from inside the source aircraft.**

The baseline AAOL turret can be configured as either a hemisphere, a hemisphere with a cylindrical base, a spherically-conformal window, a flat window and some geometry changes at the base of the turret. All of these configurations were flown in the previous program at Mach numbers less than Mach 0.7 and these have all been re-flown at Mach Numbers up to Mach 0.8; these were completed in the third year. There is some discussion of the differences in later Sections. In addition, the AAOL-T program supported testing of the Air Force Research Laboratory/DARPA 40% ABC Turret. The flight campaigns are listed in Table 1. As can be seen, only the last three Campaigns were flown in the third year and only one of these was for the baseline program; however, data reduction for the one campaign in year 3 and for the two in the previous year have continued and are now continuing along with planning for the next campaign. It should not be forgotten that the program also includes computational work and testing in wind tunnels. At this writing we are testing mitigation devices and techniques that will be flown in our next campaign. The progress on computational efforts will be covered in a later Section.

TABLE 1

## AAOL-T Flight Campaigns

- |       |  |
|-------|--|
| I.    | Safety of Flight and Unsteady Pressure                                   |
|       | • 4 Sorties, February 24 - 28, 2014                                      |
| II.   | RVSM Certification Test Flights<br>(Reduced Vertical Separation Minimum) |
|       | • 2 Sorties, March 3 – 6, 2014   |
| III.  | Optical Data   |
|       | • 5 Sorties, April 16-24, 2014   |
| IV.   | ABC 40% Turret   |
|       | • 8 Sorties, June 12 – 19  |
| V.    | ABC 40% Turret   |
|       | • 14 Sorties, August 15 – 25   |
| VI.   | Optical Data   |
|       | • 7 Sorties, September 16 – 18, 2014                                     |
| VII.  | ABC 40% Turret   |
|       | • 12 Sorties, October 8 – 22, 2014                                       |
| VIII. | Optical Data   |
|       | • 5 Sorties, March 23 -27, 2015  |
| IX.   | ABC 40% Turret   |
|       | • 5 Sorties, April 21 – 24, 2015   |
| X.    | ABC 40% Turret   |
|       | • 9 Sorties, August 26 – 31, 2015  |

### III. AERO-OPTICAL INVESTIGATION OF TRANSONIC FLOW FEATURES AND SHOCK DYNAMICS ON HEMISPHERE-ON-CYLINDER TURRETS

Flow over turrets is considered to enter the transonic flow regime for Mach numbers greater than 0.55 [6,7]. Above this critical Mach number, flow becomes locally supersonic on the turret. These locally supersonic flow regions can affect the various flow features on the turret. Figure 3 shows the flow features on a turret in the transonic regime. The most notable difference from a turret in subsonic flow is the presence of a local shock on the turret. The exact location and behavior of this shock is dependent on the freestream Mach number [5,8,9]. This shock also can induce separation downstream of it, either causing premature wake formation or locally introducing additional optically-aberrating turbulence. Other than the presence of the shock, many subsonic flow features around the turret are still present in the transonic regime. A necklace vortex forms as the boundary layer rolls up near the base of the turret and extends downstream. Whether induced by the shock or the adverse pressure gradient on the downstream portion of the turret, separation occurs and forms a fully turbulent wake. The upstream portion of the turret exhibits little turbulence, as the accelerating flow remains attached and boundary layer is thin.

It is difficult to study realistic-size turrets at high transonic speeds in tunnels, as it requires specially-designed and expensive to run tunnels with porous walls to eliminate tunnel blockage effects. Furthermore, to perform aero-optical measurements in large tunnels is not a simple task. Our wind tunnel at Notre Dame has been modified to increase its Mach number; however, with a turret in it we have only been able to get it to approximately Mach 0.6. This is why the AAOL and AAOL-T programs were designed to study aero-optical environment in flight [10], using first

Cessna Citations and in the AAOL-T program Falcon 10 planes, capable of flying up to  $M = 0.85$ , to specifically study transonic effects in flight.

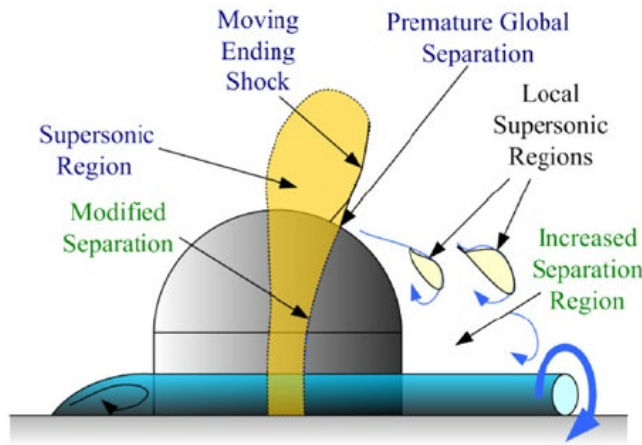


**Figure 3. Transonic flow features on the turret. From [6].**

The following subsections present results of recent aero-optical flight measurements made over years two and three of the program using the baseline AAOL turret with different aperture/window geometries over a wide range of elevation and azimuthal angles for a range of Mach numbers between 0.5 and 0.8.

**Experimental Setup.** Wavefront measurements were performed on the AAOL-T [10]. The baseline AAOL turret is 1ft. in diameter with a 4 in. cylindrical base. The turret assembly features a fast steering mirror (FSM) to stabilize the beam on the optical bench. Pictures of the turret and optical bench are shown in Figure 4 and Figure 5 shows a schematic of the optical setup in the laboratory aircraft.



**Figure 4. The AAOL turret installed on AAOL-T, left and the instrumented optical bench, right.**

Two separate flight campaigns, Campaigns VI and VIII (see TABLE 1) were conducted to investigate aero-optics of the turret with different window geometries. During the first campaign,

the optical environment around the flat-window turret was investigated at the following Mach/altitudes: 0.5/15,000 ft, 0.6/18,000 ft, 0.7/26,000 ft and 0.8/26,000 ft. During this campaign, wavefront measurements were performed using a high-speed Shack-Hartmann wavefront sensor. Similar to the data collection during AAOL program, two different acquisition modes were used for wavefronts: slewing maneuvers and fixed data. Slewing maneuvers involved the laser aircraft moving relative to the laboratory aircraft while wavefronts were continuously acquired; these maneuvers allow for rapid mapping of the optical environment around the turret [2,3]. Fixed data involved the laser plane maintaining a fixed position with respect to the laboratory aircraft. These acquisitions were performed at a higher sampling rate, as the goal of fixed data acquisitions is to investigate specific flow phenomena with a better temporal resolution. Wavefronts were collected with the spatial resolution of 32x32 subapertures and sample rates of 25 kHz for 0.7 seconds for fixed points and 3 kHz for 10-30 seconds for slewing maneuvers. Simultaneous with the 2D wavefronts, the overall beam jitter was also measured using a position sensing device. The jitter was acquired along with the turret azimuthal/elevation angle and FSM position information at 25 kHz for 10s. Flight conditions were also recorded with the wavefront and jitter measurements. The aircraft separation was measured using a differential GPS system.

During the second campaign, the turret with both the flat- and the conformal windows was flown at the following Mach/altitudes: 0.5/15,000 ft, 0.6/15,000 ft, 0.6/16,000 ft, 0.7/32,000 ft, 0.7/35,000 ft, 0.7/32,000 ft and 0.8/35,000 ft and optical data at both fixed points and slewing maneuvers were collected. During this campaign, wavefronts were collected with the better spatial resolution of 40x40 subapertures and higher sample rates of 30 kHz for fixed points and 2 kHz for slewing maneuvers. Simultaneous with the 2D wavefronts, the beam jitter was also measured using a position sensing device at 50 kHz for 30 seconds.

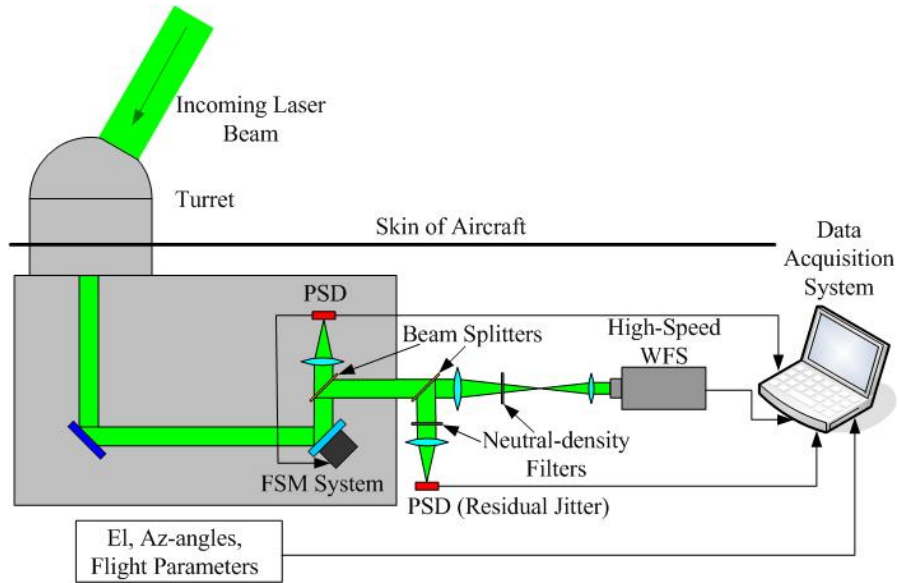


**Figure 5. Schematic of the optical setup.**

**Data Analysis.** Reducing the Shack-Hartmann images gives the measured wavefronts,  $W$ , as a function of location on the aperture and time,  $W = W(x, y, t)$ . Through least-squares plane fitting, any residual tip/tilt is removed from the wavefronts, and the steady lensing is removed by removing the mean of the wavefront at every subaperture. The optical path difference (OPD) is the conjugate of the wavefront,  $OPD(x, y, t) = -W(x, y, t)$ . To determine the variation of the OPD across



the aperture, the spatial RMS is computed at every time step,  $OPD_{RMS}(t) = \sqrt{\langle OPD(x, y, t)^2 \rangle_{(x, y)}}$ . For some aperture angles and Mach numbers, a spatial distribution of the time-averaged  $OPD_{RMS}$  at every point over the aperture,  $OPD_{RMS}(x, y)$ , was computed as,  $OPD_{RMS}(x, y) = \sqrt{OPD(x, y, t)^2}$ . The time-average  $OPD_{RMS}$ , quantifies average amount of aberration present in the beam for a specific viewing direction. Similar to subsonic aero-optical studies, [2,3], the  $OPD_{RMS}$  is normalized by the flight conditions,  $OPD_{RMS, Norm} = OPD_{RMS} / \left( \frac{\rho}{\rho_{SL}} M^2 D \right)$  to compare the aero-optical performance of the turret across various Mach numbers. In this normalization,  $\rho$  is the freestream density,  $\rho_{SL}$  is the density at sea level,  $M$  is the Mach number and  $D$  is the turret diameter. This scaling has been previously shown to collapse subsonic data acquired in flight and in the tunnel [2].

The turret azimuthal (Az) and elevation (El) angles were recast into a coordinate system that is more useful from a fluid dynamics perspective. This system uses a viewing angle,  $\alpha$ , that determines how far downstream the turret is looking and the modified elevation angle,  $\beta$ , that quantifies how far the turret is looking away from the wall of the aircraft. The viewing angle is given by  $\alpha = \cos^{-1}(\cos(Az)\cos(El))$ , and the modified elevation angle is given by  $\beta = \tan^{-1}\left(\frac{\tan(El)}{\sin(Az)}\right)$ , as shown in Figure 6.

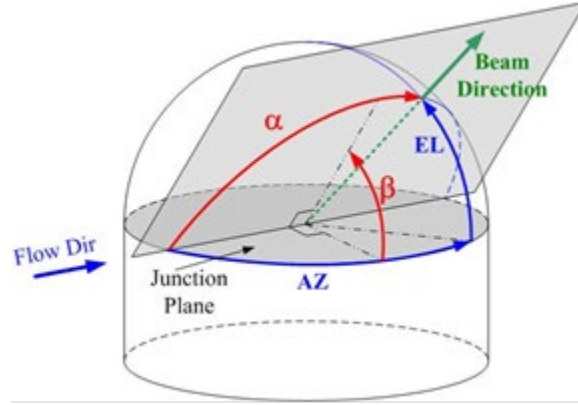


**Figure 6. Definitions of azimuthal (Az) and elevation (El) angles to viewing angle ( $\alpha$ ) and modified elevation angle ( $\beta$ ). From [2].**

**Results Flat-Window Turret.** Figure 7 shows the normalized  $OPD_{RMS}$  values for the flat-window turret as a function of Mach number and viewing angle. As  $M = 0.5$  was extensively studied during AAOL program, so only four points for  $M = 0.5$  were collected, mainly for comparison and repeatability purposes. For  $M = 0.6$ ,  $OPD_{RMS}$  values are fairly small for  $\alpha < 90^\circ$ , as the flow is attached over the flat-window aperture;  $OPD_{RMS}$  values are very similar to  $M = 0.5$  values, see [2]. Also, in [2] it was shown that at subsonic speeds over a range of viewing angles between  $90^\circ$  and  $100^\circ$ , a local separation bubble forms over the flat aperture, causing a local increase in  $OPD_{RMS}$  values. At  $M = 0.6$  the local shock on top of the turret is very weak to modify the otherwise subsonic flow over the turret, so a rather similar peak in  $OPD_{RMS}$  is present at  $M = 0.6$ ; the peak location is slightly shifted toward  $90^\circ$ . At  $\alpha = 110^\circ$  the flow separates, and for large viewing angles  $\alpha > 110^\circ$   $OPD_{RMS}$  continuously increase due to looking through the separated wake of the turret. Again, this behavior is very similar to  $OPD_{RMS}$  results at  $M = 0.5$ .

For a higher  $M = 0.7$ , the location of the local peak due to the separation bubble is around  $90^\circ$  and approximately unchanged from  $M = 0.6$ . The unsteady local peak is sharper, compared to

M=0.6 case; inspection of wavefronts have revealed the presence of the shock approximately in the middle of the aperture. The flow separates around  $110^\circ$  as well, but the wake arrears to be more optically-aberrating.

For  $M = 0.8$ , a stronger shock was found to be present over the flat aperture between viewing angles  $75^\circ$  and  $90^\circ$ , so the overall levels of  $OPD_{RMS}$  are significantly higher, compared to values at the same angle range at lower Mach numbers. The shock was found to be unsteady and moving approximately in the middle of the aperture, see spatial distributions of  $OPD_{RMS}$  for shock-induced wavefronts in Figure 8. The flow separation is also affected by the shock presence and appears to occur slightly upstream, at  $\alpha = 105^\circ$ , compared to  $M = 0.6$  and  $M = 0.7$ . There is no local peak that is indicative of a separation bubble for  $M = 0.8$ , indicating that the shock-induced separation over the flat-window prevents its formation.

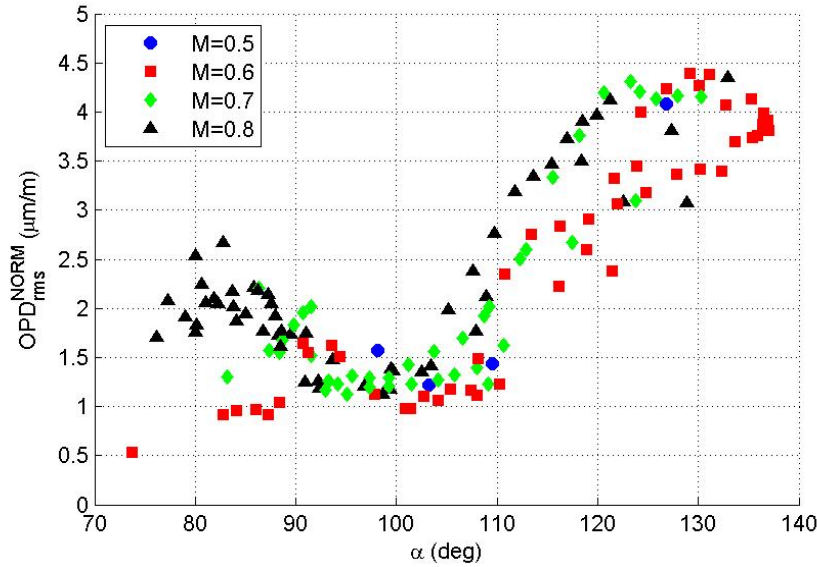


**Figure 7. Normalized  $OPD_{RMS}$  versus viewing angle for  $M = 0.5-0.8$  for the flat-window turret.**

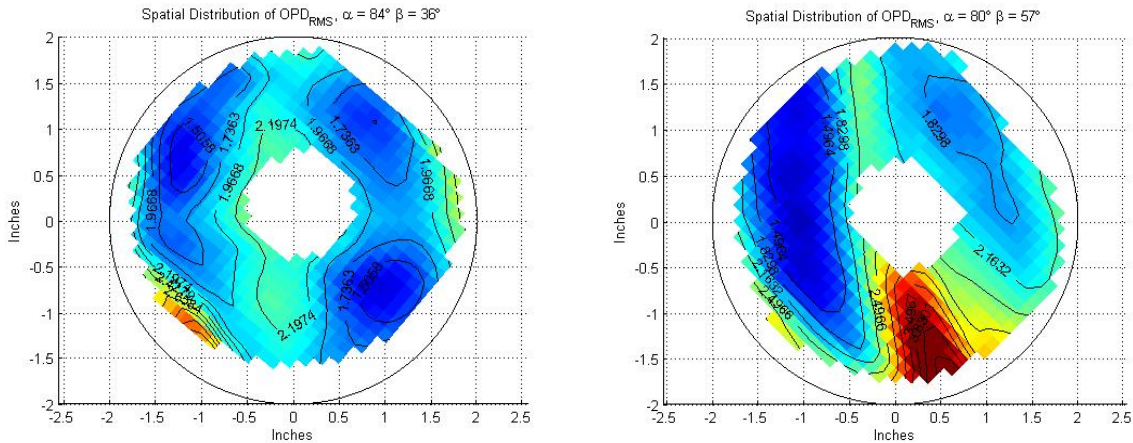


**Figure 8. Spatial Distributions of  $OPD_{RMS}$  for the flat-window aperture. Left:  $Az = 82^\circ$  and  $El = 36^\circ$  ( $\alpha=84^\circ$ )  $M = 0.7$ . Right:  $Az = 72^\circ$  and  $El = 56^\circ$  ( $\alpha=80^\circ$ )  $M = 0.8$ . Flow goes from left to right.**

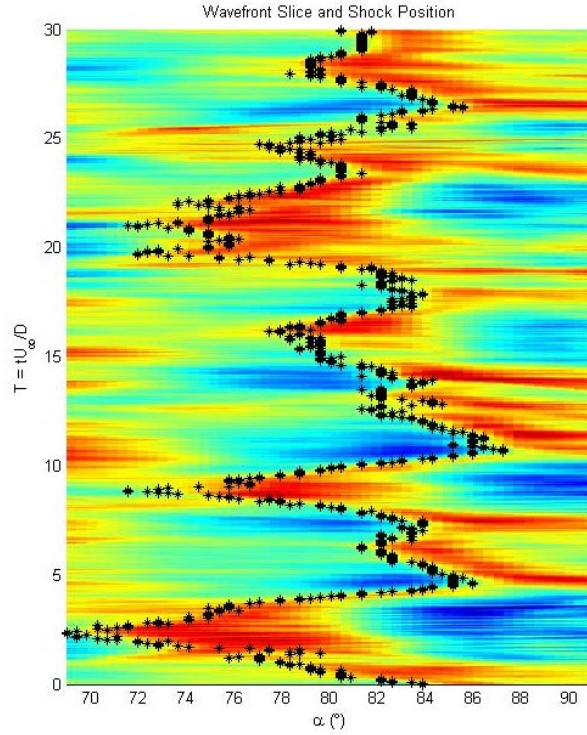


**Figure 9: Spatial-temporal evolution of 1-D slice of wavefront for  $M = 0.8$  for aperture located at  $\alpha = 80^\circ$ ,  $\beta = 43^\circ$ . Black circles indicate the approximate shock location.**

The normalized spatial distributions of  $OPD_{RMS}$  are shown in Figure 8. Both the  $M = 0.7$  wavefronts, left and  $M = 0.8$  wavefronts, right show an increase in  $OPD_{RMS}$  in a narrow band near the center of the aperture due to the presence of the unsteady shock. This is the shock location for both cases. Because the shock location is near the center of the aperture, even though the viewing angle and Mach number are slightly different between the two cases, it is believed that the flat window has an “anchoring” effect on the shock in that it forces it to the center of the aperture, on average. One possible reason for this “anchoring” effect is that the separation bubble forms a fluidic curved surface over the aperture. The topology of the separation bubble is very sensitive to the flat-window position, as well as the flow environment. For  $M = 0.7$  the shock is formed over the curved fluidic surface, but the shock is fairly weak to modify it. The shock becomes much stronger at  $M = 0.8$ , essentially destroying the bubble. As it will be shown later in this paper in Figure 10, the resulted  $OPD_{RMS}$  for both the flat- and the conformal-window aperture are very similar at  $M = 0.8$ , confirming that the aperture geometry becomes a secondary factor, compared to the shock-induced effects.

Figure 9 shows a one-dimensional slice of wavefronts taken at  $M = 0.8$  for the aperture located at  $\alpha = 82^\circ$  and  $\beta = 43^\circ$ . The shock location was captured in  $\alpha$ - $\beta$  coordinates for given fixed  $\beta$ . The discontinuity of a shock causes a sharp change in the wavefront, so shock tracking was done by stepping along  $\alpha$  at the  $\beta$  of interest to find the location of maximum slope in the  $OPD_{RMS}$ ; a similar analysis was performed to study the shock dynamics on a 2D turret in the wind tunnel in [4,5]. The black filled circles show the location of maximum positive wavefront slope, which is presumed to be related to the instantaneous shock position. This maximum slope corresponds to the location of the shock. The shock moves between a relatively wide range of  $\alpha = 70^\circ$  and  $88^\circ$ ; this unsteady shock motion is as a cause of the increase in  $OPD_{RMS}$  observed in the  $M = 0.8$  data from Figure 5. The shock movement, although oscillatory, doesn’t appear to be periodic in nature and the shock does not “wander” off of the aperture.



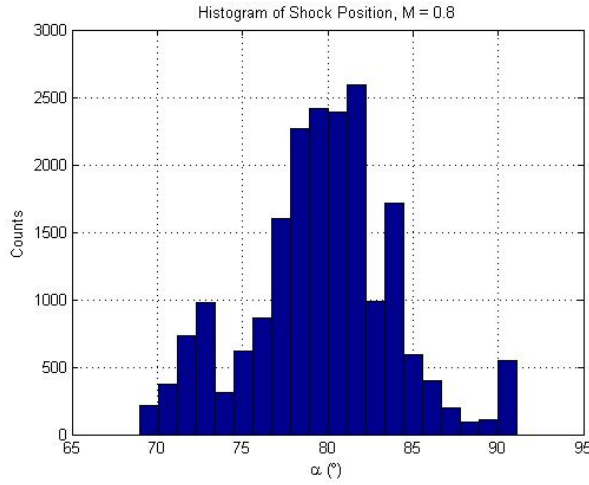


**Figure 10: Histogram of the shock position for  $M = 0.8$  at  $Az = 72^\circ$ ,  $El = 56^\circ$ .**

The histogram of the shock position for  $M = 0.8$  is shown in Figure 10. The shock is between  $71^\circ$  and  $87^\circ$  90% of the time, and the average location is at  $80^\circ$ . For  $M = 0.7$  (not shown), the shock moves approximately the same amount as for  $M = 0.8$ .

The spectra of the shock position for both  $M = 0.7$  and  $M = 0.8$  are shown in Figure 11. There isn't much discernable difference between the frequency content of the shock movement for the two Mach numbers. Both exhibit a peak near  $St = 0.15$  and fall off after that. This peak has been associated with the movement of the separation line on a hemisphere on cylinder turret for subsonic [11] and transonic [12] flow regimes. As the separation bubble is sensitive to the global environment, which is primarily governed by the separated region downstream of the turret, this single peak in the shock spectra indicates that the shock dynamics is linked to the separation line dynamics.

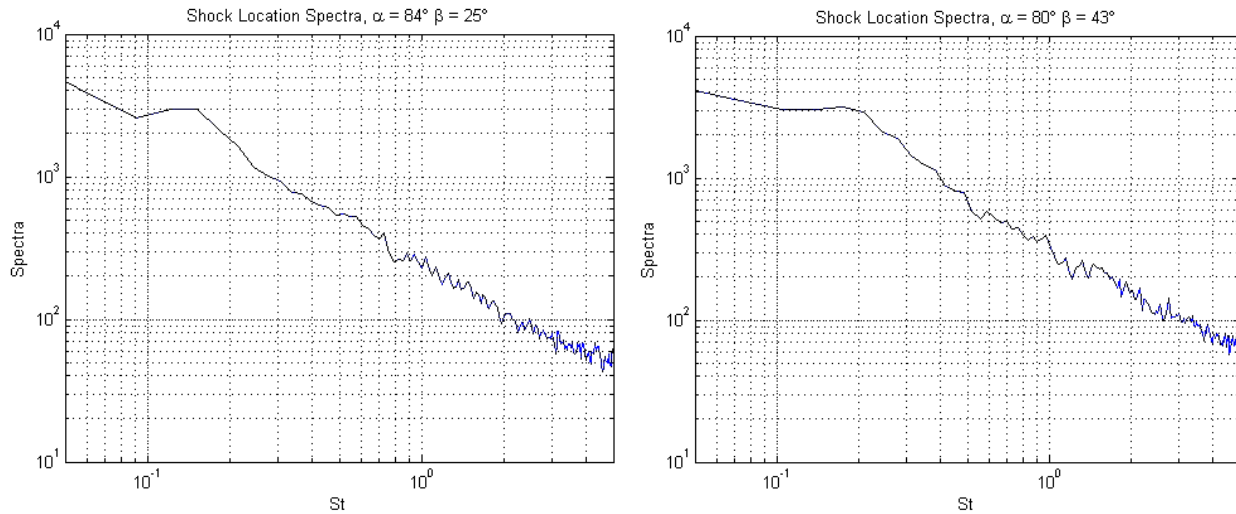


**Figure 11: Shock location spectra for  $M = 0.7$ , left and  $M = 0.8$ , right.**

**Results Conformal-Window Turret.** Figure 12 shows the normalized  $OPD_{RMS}$  values for the conformal-window turret as a function of Mach number and viewing angle. At subsonic Mach numbers of 0.5 and 0.6, the flow is subsonic everywhere around the turret. Unlike for the flat-window turret, shown in Figure 5, the flow stays attached over the aperture for side-looking angles  $80$ - $90$  degrees with the low resulting  $OPD_{RMS}$ , as the conformal-window does not trip the flow around the aperture. For higher Mach numbers of 0.7 and 0.8 the unsteady shock appears over the

aperture at the viewing angle of approximately 80 degrees, resulting in a local increase of  $OPD_{RMS}$ . Optical distortions at looking-back angles,  $\alpha > 100$  degrees, are due to the wake downstream of the turret and are similar for both the flat- and conformal-window turrets, see Figure 7 for comparison.

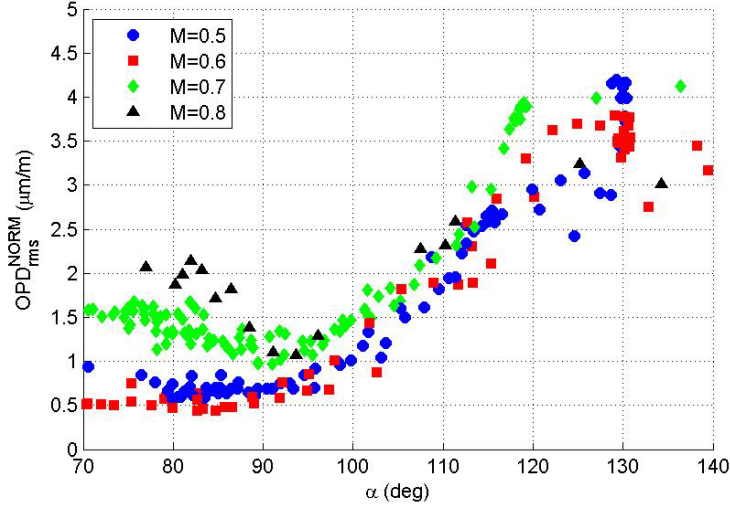


**Figure 12. Normalized  $OPD_{RMS}$  versus viewing angle for  $M = 0.5-0.8$  for the conformal-window turret.**

To visualize the shock location on the turret, spatial distribution of  $OPD_{RMS}$  over the aperture at side-looking angles were projected on the turret. The shock creates additional localized distortions and it is visible as a line of the increased distortions, as shown in Figure 13. The average shock location is around  $\alpha = 80$  degrees and fairly independent of the modified elevation angle. The streamwise shock extent increases with the Mach number increase.

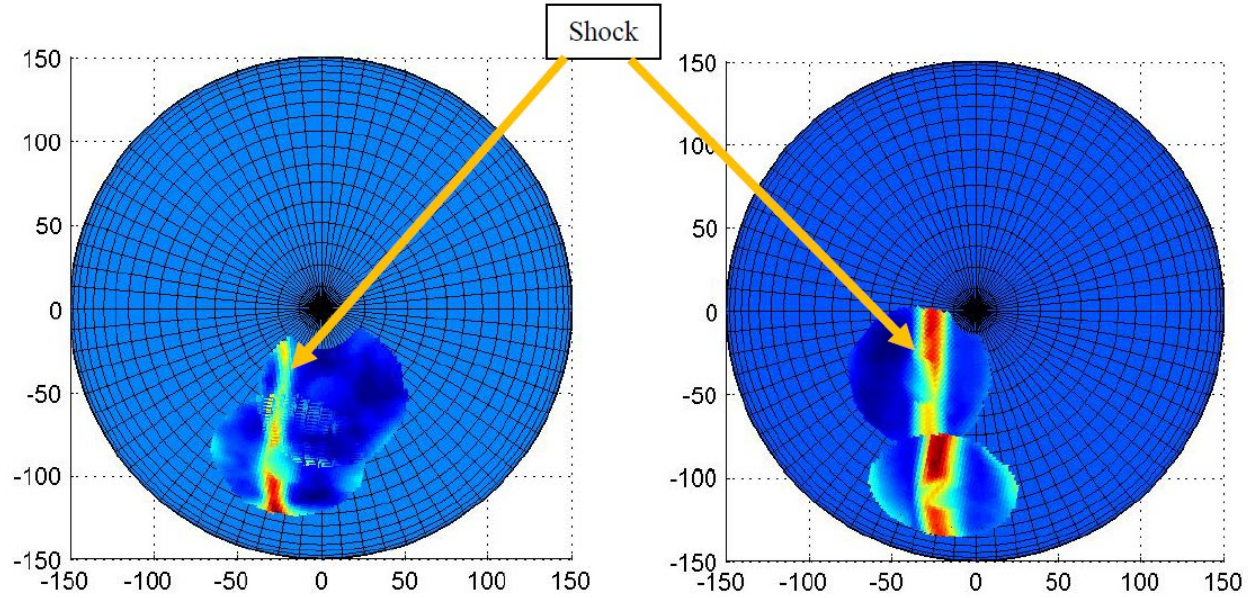


**Figure 13. The top view of spatial variation of wavefronts for side-looking angles, indicating the shock location for  $M=0.7$  (left) and  $M=0.8$  (right). Flow goes from left to right.**

To further study the temporal shock dynamics, spatial-temporal evolution 1-D slices of the wavefronts were extracted at different  $\beta$ -locations and Mach numbers and the instantaneous shock location was extracted, as it was described before. Figure 14 shows temporal evolution of a one-

dimensional slice of the wavefront for a conformal window turret taken at  $M = 0.7$  and  $M = 0.8$  with  $\beta = 60^\circ$  and  $\beta = 50^\circ$ , respectively. The black dots represent the shock location for each time step. The shock motion is not periodic for either case, although the shock for  $M = 0.8$  clearly has a single preferred frequency. Shocks are present consistently for each Mach number. The shock location for  $M = 0.7$  varies from  $74^\circ$  to  $83^\circ$ , while for  $M = 0.8$  it has a larger range of  $70^\circ$  to  $84^\circ$ . The  $M = 0.8$  case also has a larger non-dimensional time between peaks than the  $M = 0.7$  case, indicating a lower oscillation frequency content.

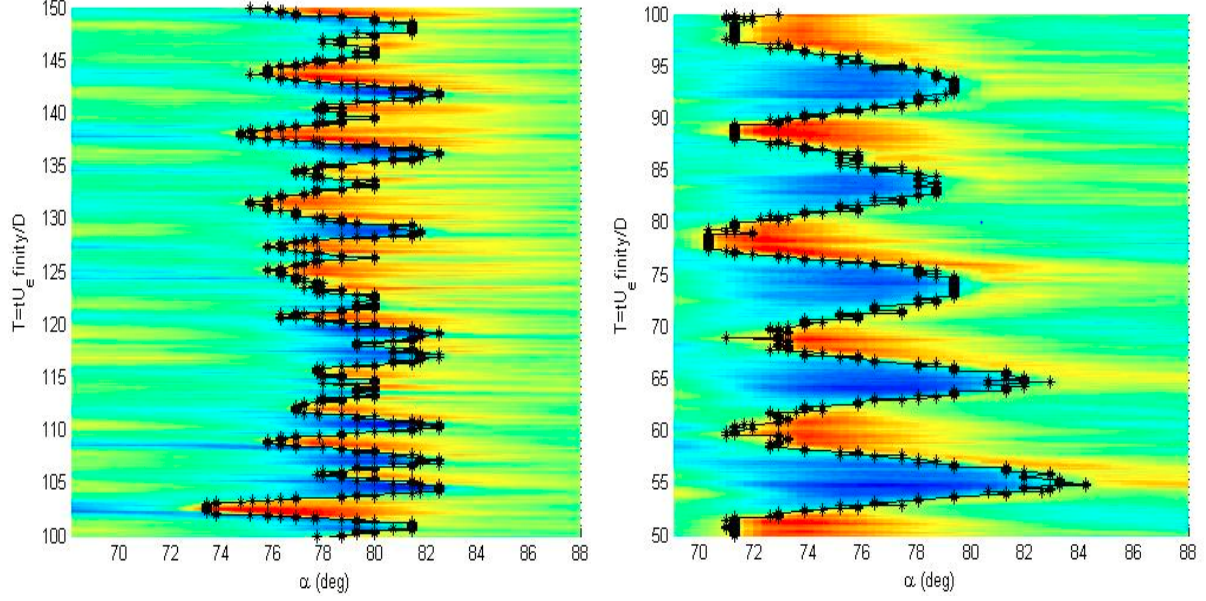


**Figure 14: Spatial-temporal evolution of 1-D slice of wavefront data with  $M = 0.7$  (left) at  $\beta = 60^\circ$  and  $M = 0.8$  (right) at  $\beta = 50^\circ$ . Black circles indicate the approximate shock location.**

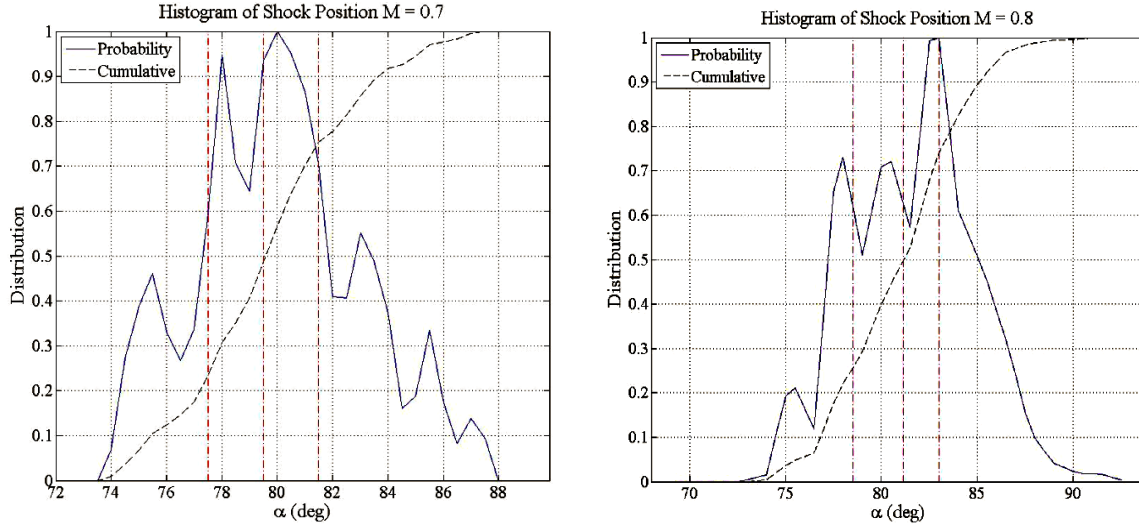


**Figure 15: Probability and Cumulative Distribution Functions of shock locations at  $\beta = 70^\circ$**

Figure 15 shows the probability and cumulative distributions of the shock angles for  $M = 0.7$  and  $M = 0.8$  at the same  $\beta$  location. In both cases the probability function is not symmetric. The shock location ranges from  $74^\circ$  to  $88^\circ$  at  $M = 0.7$ , while in the  $M = 0.8$  case it has a larger range of  $70^\circ$  to  $92^\circ$ . Figure 16 depicts the median shock locations at different  $\beta$ -angles with bars representing the range of  $\alpha$  where the shock is present 90%. The median shock location angle does not change



significantly with changing  $\beta$  for either Mach number, which is consistent with the spatial distribution of  $OPD_{RMS}$  in Figure 13. For  $M = 0.8$  the shock tends to have a larger range than for  $M = 0.7$ .

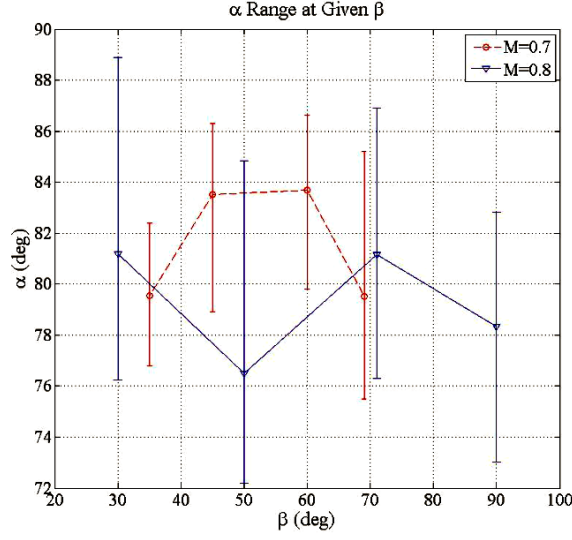


**Figure 16: Shock median locations and 90%-range for  $M = 0.7$  and  $M = 0.8$  for conformal-window turret.**

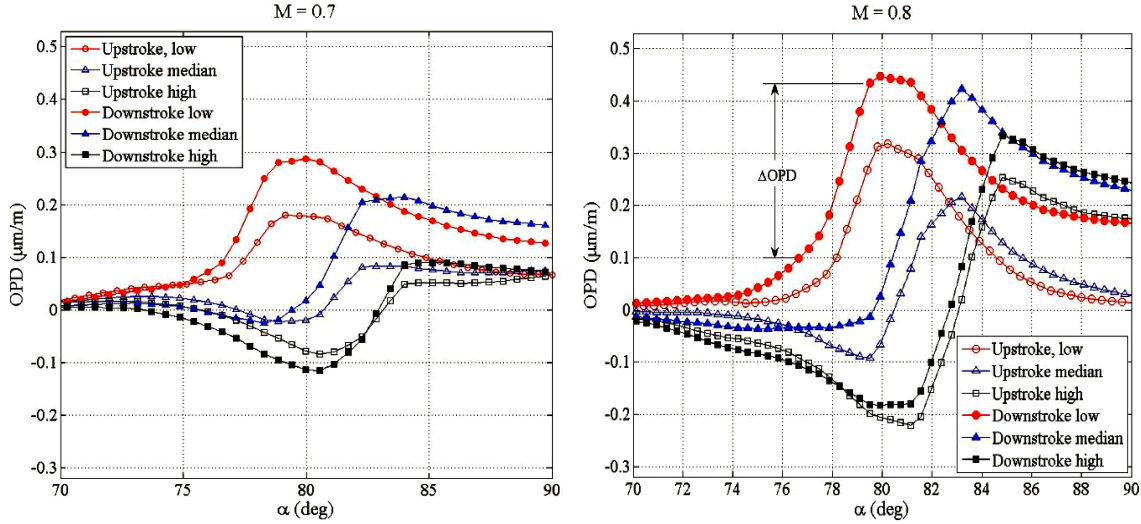


**Figure 17: Averaged One-dimensional wavefronts for shock incidences at viewing angles and  $\beta = 70^\circ$ .**

Figure 17 shows one-dimensional mean wavefronts located at the viewing angles corresponding to the locations marked by red dotted lines in Figure 15. At these  $\alpha$ -locations the cumulative probability reaches 25% (upstream of the median), 50% (median) and 75% (downstream of the median). These points were selected to represent the wavefront shape and shock dynamics at various moments of the shock motion for each Mach number. They were found by conditionally-averaging all of the instantaneous wavefronts with shocks located at the corresponding viewing angle. The analysis was done separately for time steps where the shock was moving toward higher  $\alpha$  (downstroke), and toward lower  $\alpha$  (upstroke). The shock optical strength at a given angle was determined by finding the change in OPD across the sharp gradient region in the one-dimensional wavefront, as shown in Figure 17, right. Bounds of the shock were considered to be where the OPD slope was 70% of the maximum slope of the wavefront. The shock strength is consistently greater at

$M = 0.8$ , and during the upstroke motion the shock was found to be stronger than during the downstroke motion at each Mach number. The change in OPD is almost constant at  $M = 0.7$  with varying viewing angle, while at  $M = 0.8$ , there is a larger jump in OPD at higher angles.

To illustrate this effect, Figure 18 depicts the average shock strength for both the upstroke and the downstroke motion for different  $\alpha$  at  $M = 0.7$  and  $0.8$ . The range of  $\alpha$  contains 90% of the data. For  $M = 0.7$  the shock strength is almost constant over the range of the viewing angles, but for  $M = 0.8$  the shock strength increases as  $\alpha$  increases. The upstroke shock strength is consistently higher than the downstroke for both cases. A similar shock behavior was seen in AAOL at  $M = 0.65$  [3] and around cylindrical turrets [5], where the shock during the upstroke motion was also found to be stronger, compared to the downstroke motion. In [3] it was proposed that the stronger upstroke shock strength is linked to fluctuations in the separation bubble size. Presented results seem to support this proposition.

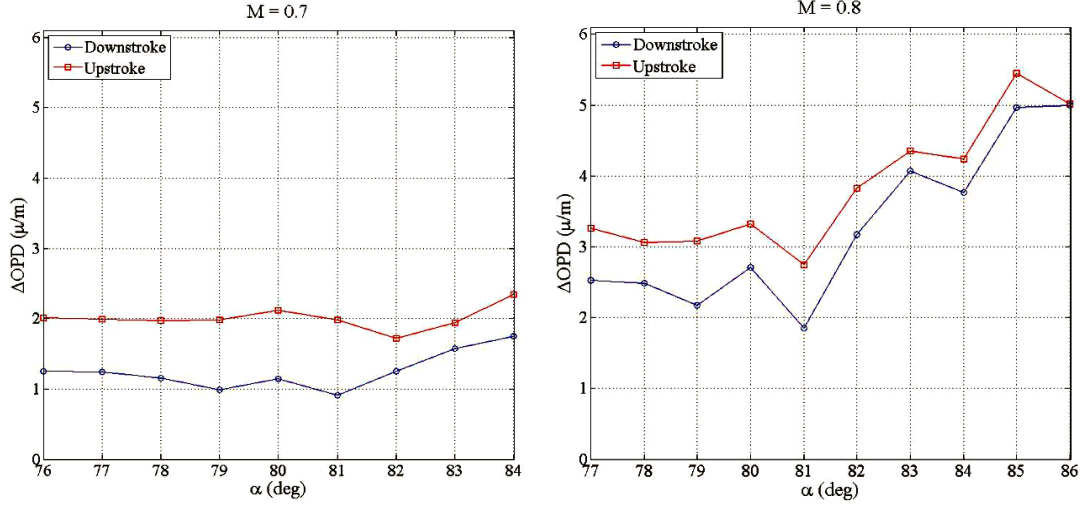


**Figure 18: Average Shock Strength Determined Change in OPD Across the Shock at  $\beta = 70^\circ$  and  $M = 0.8$**

The temporal spectra of the shock position for a conformal window at  $M = 0.7$  and  $M = 0.8$  are shown in Figure 19. The most discernable difference between the two is that the  $M = 0.7$  case has peaks around  $St = 0.18$  and  $St = 0.3$ , while the  $M = 0.8$  case has only one peak near  $St = 0.15$ ; this lower-frequency dynamics was already observed in Figure 14.

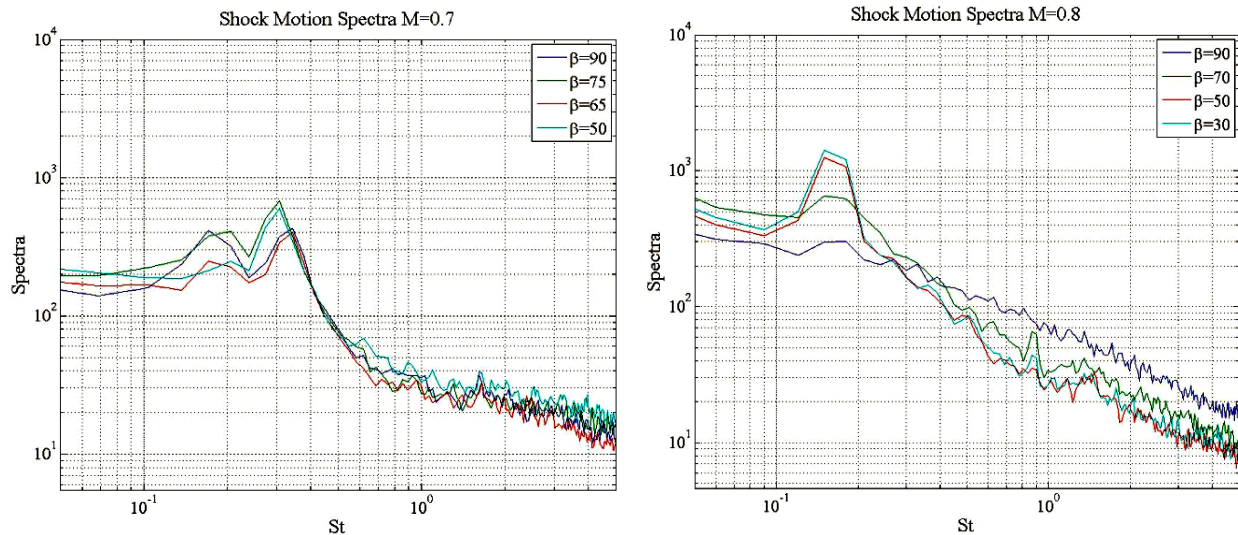


**Figure 19: Conformal-Window shock location spectra for  $M = 0.7$ , left and  $M = 0.8$ , right.**

Results from pressure measurements on AAOL turret [12] have showed similar peak locations for both  $M = 0.7$  and  $0.8$ . To understand a possible mechanism of this low-frequency dynamics, let us recall that a weaker, intermittent shock was observed on the AAOL at a lower  $M = 0.65$  [3] with a typical frequency of  $St \sim 0.5$ . Also,  $St = 0.15$  has been associated with the unsteady separation line motion over a wide range of subsonic [11] and transonic [12] Mach numbers. So, while at low transonic speeds the shock dynamics is mostly independent of the separation region dynamics, at higher Mach number the shock becomes strong enough to force a premature separation, effectively coupling or locking-in the shock and the separation line dynamics. In [5] this strong coupling between the shock location and its strength with the location and the size of the separated region was studied over cylindrical turrets and an acoustical feedback was proposed as a possible mechanism for locking the dynamics of the shock and the shock-induced separation region.

**Wavefront Spectra in the Wake.** To investigate the possible effects of the shock, formed on the turret, on the optical performance of the separated wake, aperture-averaged normalized wavefront spectra were computed for the viewing angle of  $\alpha = 120$  degrees for different Mach numbers and window geometries and the results for the flat-window turret are shown In Figure 20, left, and for the conformal-window turret in Figure 20, right. For high viewing angles, the beam traverses through the separated region, dominated by the shear-layer structures. Spectra for all Mach numbers, including transonic ones, show a very good collapse for both window geometries. The peak in spectra is around  $St_D = 1.3$ , which corresponds to a typical normalized frequency for the shear layer structures at subsonic speeds at these viewing angles [20]. The spectra collapse indicates that once the flow is separated, the presence of the shock does not significantly affect the structures in the separation region. Nevertheless, note that for the highest measured  $M = 0.8$ , the small secondary, separation-line-related peak appears around  $St_D = 0.15$  for both window geometries; this is also consistent with the lock-in mechanism between the shock and the separation region, discussed above.

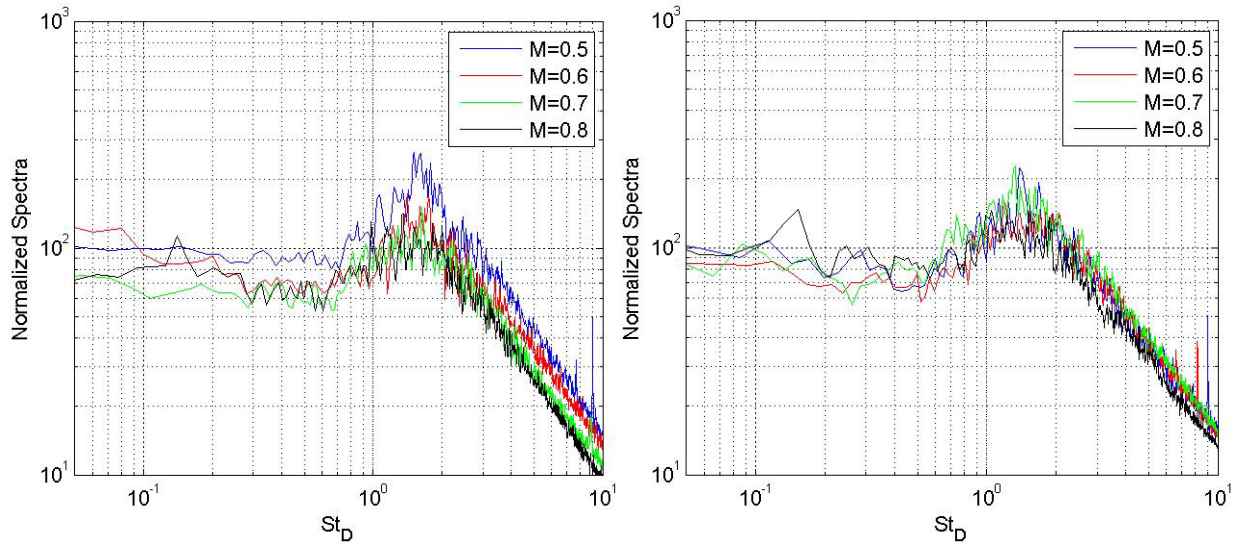


**Figure 20. Normalized aperture-averaged wavefront spectra for several Mach numbers for  $\alpha = 120$  degrees for the flat-window (left) and the conformal-window (right) turrets.**

#### IV. TRANSONIC FLOW DYNAMICS OVER A HEMISPHERE IN FLIGHT

There are many applications for optical turrets operating on airborne platforms at transonic speeds [6]. However, the optical distortions associated with the flow features around a turret such as an unsteady shock and flow separation, reduce the beam quality [6]. In order to reduce or eliminate optical aberrations it is necessary to better understand the transonic flow features over a hemispherical turret.

Aero-optical effects in the fully subsonic regime have been thoroughly studied and are well understood [1,2,3,6,14,15,16], but at Mach numbers above 0.55 the flow becomes locally supersonic near the top of the turret, resulting in an unsteady local shock and earlier shock-induced flow separation [5,6]. The presence of the shock and early separation point not only increase the amount of optical distortion as discussed in the earlier Section, but it also give rise to unsteady pressure disturbances that find their way into the beam train and induce aero-induced jitter.

Pressure and optical measurements have previously been performed on hemisphere-on-cylinder turrets in flight [1,14]. In the AAOL-T program and, we measured unsteady pressure on the baseline AAOL turret in higher, transonic speeds and in particular over the turret configured as a hemisphere-only turret. Both numerical simulations [17,18] and wind tunnel experiments [16] have been performed with hemispheres to better understand the shock and boundary layer effects on optics. In this Section the study is extended to flight testing.

The interaction between the shocks and the separated wake region over bodies with large spanwise curvature is not yet fully understood [9-11]. Measuring the pressure field over the hemisphere surface gives insight into the shock and boundary layer motion from a non-optical point of view. Since both the shock and flow separation are detrimental to beam quality [1,2,13,14], it is important to gain a better understanding of the interaction between them. This knowledge will enable adaptive feedback mechanisms and flow control that will mitigate unwanted aero-optical effects [12].

**Experimental Setup.** Unsteady local pressure measurements [19] were performed in February of 2014 during in-flight safety of flight testing but have only been analyzed in conjunction with optical data during the 3<sup>rd</sup> year. The 12-inch diameter AAOL baseline turret was configured as a hemisphere-only and mounted on the Falcon 10 aircraft, see Figure 21, left. The turret was mounted on a frame that allowed for rotation to any desired azimuthal angle and featured a worm-gear system that allowed control the of elevation angle, see Figure 22, right. The hemispherical turret was with 19 pressure sensors on it, shown in Figure 22. The pressure sensors were Kulite differential pressure transducers and were placed approximately uniformly over the entire surface of the hemisphere with a cluster of 7 points centered over the aperture as shown in figure 2. Data was collected for 12 different azimuthal angles between 0 to 180 degrees; the elevation of the aperture was fixed at 45 degrees. Data sets were collected at 15,000 feet for Mach numbers of 0.4, 0.5, 0.6, and 28,000 feet for Mach numbers of 0.7, and 0.8, see TABLE 1 for details; the zero azimuthal angle aligned with the incoming freestream flow. The data were collected at a sampling rate of 25 kHz for 20 seconds during each data set.

Corresponding optical measurements were taken on the AAOL-T in March of 2015 with the optical turret recessed into the aircraft, so only the hemispherical portion of it sticking out, see Figure 23, left.



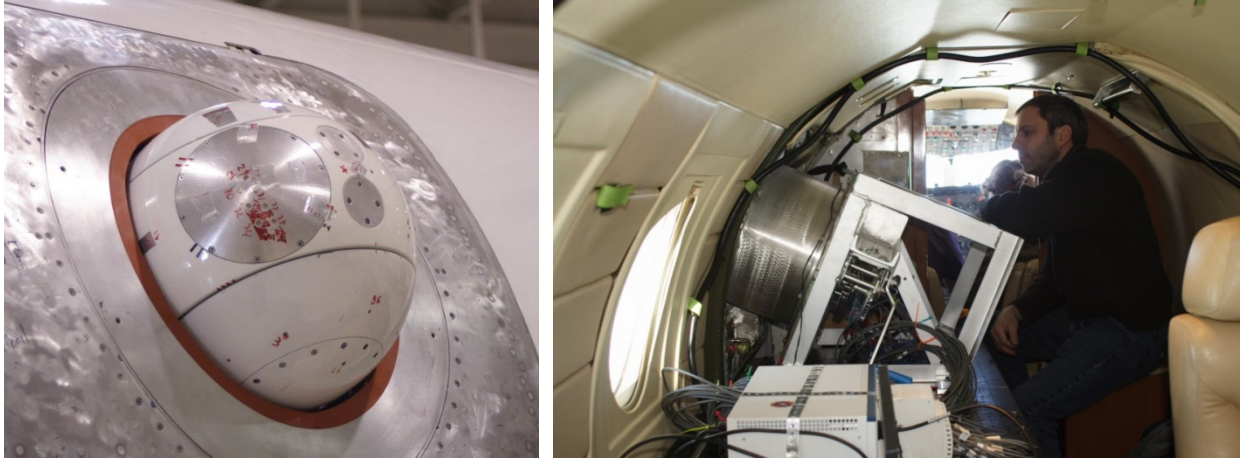


**Figure 21: The pressure-instrumented hemispherical turret with the conformal window mounted on the AAOL-T, left and the interior testing bench, right.**

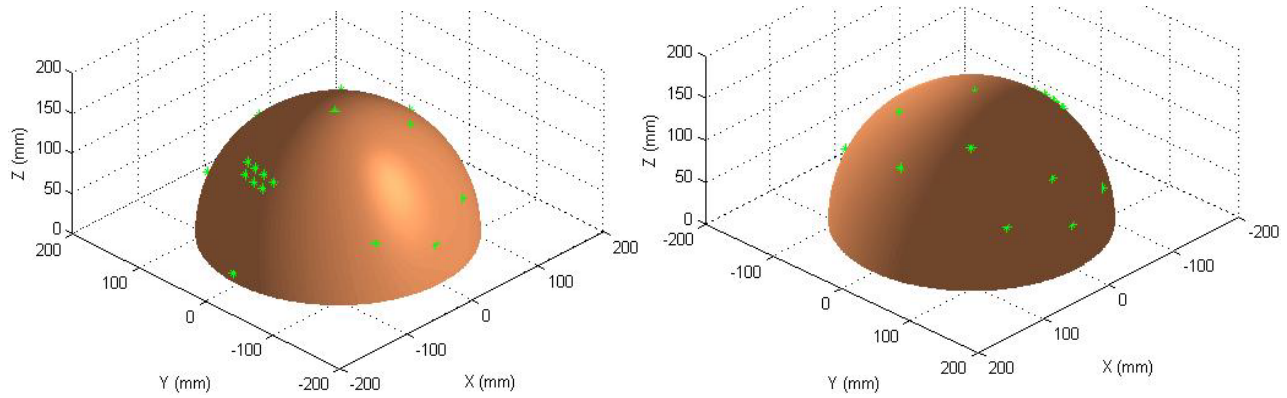


**Figure 22. Pressure Port Locations for a single azimuthal angle**

**TABLE 1**  
**Flight conditions and azimuthal angles for hemispherical turret**

Altitude/Mach and Az-anlges (in degrees)	
15 kft/0.4:	Az = 0 8 20 28 44 90 134 180
15 kft/0.5:	Az = 0 8 20 28 44 90 134 180
15 kft/0.6:	Az = 0 8 20 28 44 85 88 90 134 180
28 kft/0.7:	Az = 0 8 20 28 44 85 88 90 112 134 180
28 kft/0.8:	Az = 0 8 20 28 44 85 88 90 97 112 134 180

The optical setup in the laboratory aircraft was described in detail in [20,21] and described in a previous section, see Figure 4, right, for a photo of the optical bench. Figure 21, showing the hemisphere-only turret configuration, can be compared with Figure 4 that shows the baseline AAOL turret in the hemisphere on a cylindrical base configuration. Wavefront measurements were performed using a high-speed Shack-Hartmann wavefront sensor as described in an earlier Section. The wavefront sensor featured 32x32 subapertures at a sample rate of up to 25 kHz. Simultaneous with the 2D wavefronts, the beam jitter was also measured using a position sensing device. The



jitter was acquired with the turret viewing angle and FSM position information at 25 kHz for 10s. Flight conditions were also obtained simultaneous with the wavefront and jitter measurements. The aircraft separation was measured using a differential GPS system.

Two different acquisition modes were used for wavefronts: slewing maneuvers and fixed data. Slewing maneuvers involved the laser aircraft moving relative to the laboratory aircraft while wavefronts were continuously acquired at 3 kHz for at least 15 seconds. These maneuvers allow for rapid mapping of the optical environment around the turret [1,2]. Fixed data involved the laser plane maintaining a fixed position with respect to the laboratory aircraft. These acquisitions were performed at a higher sampling rate of 25 kHz for 0.7 seconds. The goal of fixed data acquisitions is to investigate specific flow phenomenon with a better temporal resolution.



**Figure 23: The AAOL turret installed on AAOL-T.**

**Data Analysis.** The pressure data from multiple hemisphere orientations were combined to find pressure data over a range of viewing angles. The pressure was normalized by the dynamic pressure to get the pressure coefficient,  $C_p = \frac{p - p_{ref}}{\frac{1}{2} \rho U^2}$ , where  $\rho$  is the freestream density and  $U$  is the

freestream velocity. Calculating the root mean square determines the temporal variation of the pressure coefficient at each location,  $Cp_{RMS}(t) = \sqrt{Cp(t)^2}$ . The pressure spectra were calculated to compare the frequency with both pressure and optical data from other experiments.

The Shack-Hartmann images were reduced using in-house software to obtain the wavefronts,  $W$ , as a function of location on the aperture and time,  $W = W(\bar{x}, t)$  as described in a previous Section.

**Optical results.** Figure 24 shows the normalized  $OPD_{RMS}$  values as a function of Mach number and viewing angle. As  $M = 0.5$  was extensively studied during AAOL program [3], only several points for  $M = 0.5$  were collected, mainly for comparison and repeatability purposes. For  $M = 0.6$ ,  $OPD_{RMS}$  values are fairly small for  $\alpha < 110^\circ$ , as the flow is attached over the flat-window aperture;  $OPD_{RMS}$  values are very similar to  $M = 0.5$  values. At  $\alpha = 110^\circ$  the flow separates, so for large viewing angles  $\alpha > 110^\circ$   $OPD_{RMS}$  continuously increase due to looking through the separated wake of the turret. Again, this behavior is very similar to  $OPD_{RMS}$  results at  $M = 0.5$ .

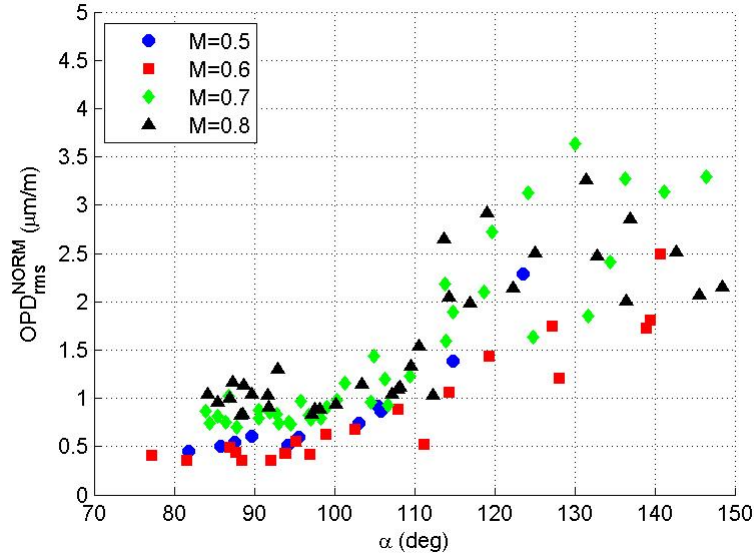


**Figure 24: Normalized OPDRMS versus viewing angle for  $M = 0.5-0.8$ .**

For a higher  $M = 0.7$ , a small unsteady shock appears near  $\alpha = 90$  degrees, thus increasing the local aero-optical distortions near this viewing angle. The flow separates around  $110^\circ$  as well, but the wake arrears to be more optically-aberrating. For  $M = 0.8$ , the shock intensifies, so the overall levels of OPDRms are higher, compared values at the same angle range at lower Mach numbers. The shock dynamics was found to be similar to the shock dynamics over the hemisphere-on-cylinder turret [20]. Overall, the aero-optical distortions over the hemispherical turret were found to be weaker than for the hemisphere-on-cylinder turret, compare with Figure 12.

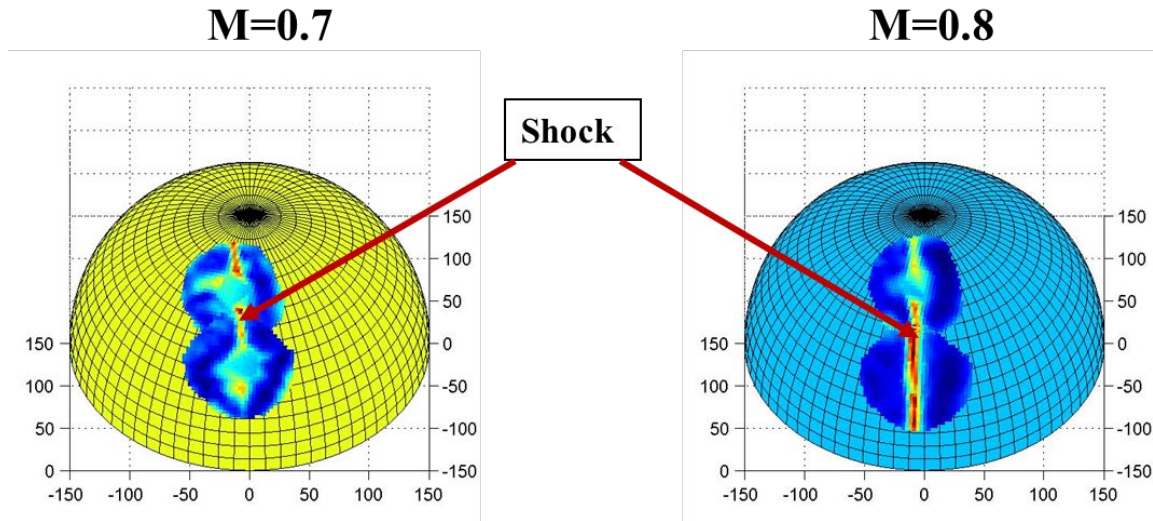


**Figure 25. Spatial variations of the wavefronts over the aperture,  $W_{rms}(\alpha, \beta)$ , projected on the turret for  $M = 0.7$  (left) and  $M = 0.8$  (right). Flow goes from left to right.**

To visualize the shock location on the turret, spatial variations of wavefronts at side-looking angles were projected on the hemispherical turret. Results for  $M = 0.7$  and  $0.8$  are presented in Figure 25. The shock creates additional localized distortions, visible as a line of the increased distortions. The average shock location is around  $\alpha = 88$  degrees and fairly independent of the elevation angle, consistent with tunnel tests [23] and numerical simulations [24,25].

Temporal evolution of the wavefronts was used to calculate aperture-averaged wavefront spectra. An example of the spectra for a side-looking angle of  $\alpha = 90$  degrees for  $M = 0.6, 0.7$  and  $0.8$  are shown in Figure 26, left. The increase in spectra increase in the frequency range  $St_D = 0.1-1$  at  $M = 0.7$  and  $0.8$  due to the shock appearance is clearly visible. These shock-related spectra have two peaks near  $St = 0.15$  and  $0.3$ . The first peak at  $St = 0.15$  has been associated with motion of the separation line [23], the second peak at is the strongest for  $M = 0.7$ , while the first peak become stronger at  $M = 0.8$ . This indicates a coupling or locking-in of the shock and separation line at high transonic speeds; this lock-in mechanism was also observed in relevant tunnel tests at transonic speeds [5]. Wake-related spectra at  $\alpha = 125$  degrees for range of Mach numbers are shown in Figure 26, right, and exhibit self-similar behavior with a peak at higher frequency of around  $St_D = 1.3$ . Thus, the presence of shock does not affect shear-layer-type structures in the separation region.

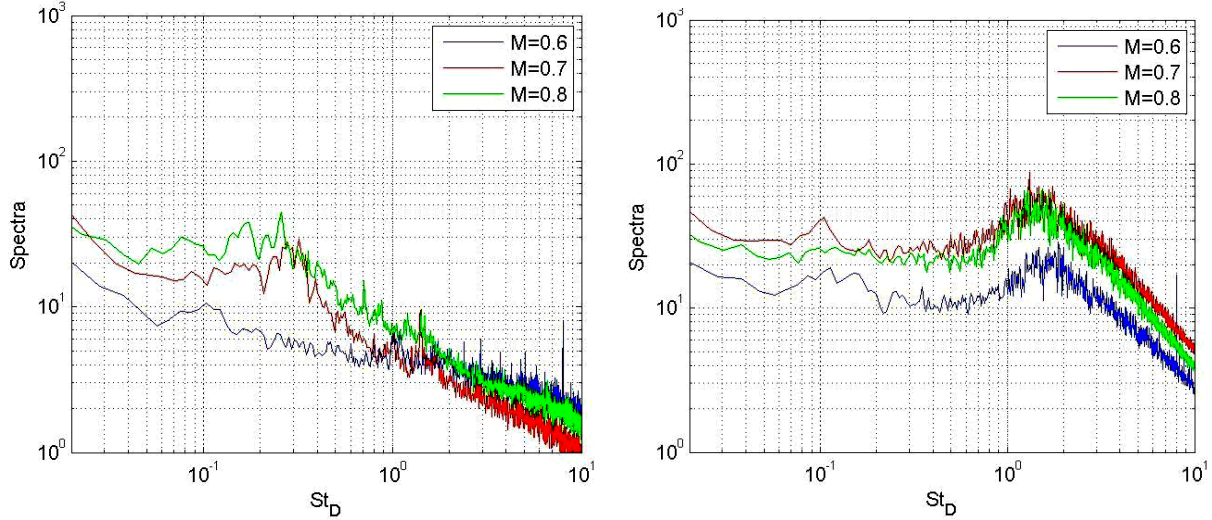


**Figure 26. Normalized, aperture averaged wavefront spectra for  $\alpha = 90$  degrees, left, and  $\alpha = 125$  degrees, right, for incoming  $M = 0.6, 0.7$  and  $0.8$ .**

**Pressure Results.** The Optical results were presented in a previous Section; however here the data are augmented to compare with unsteady pressure data with temporal evolution of the wavefronts. The root mean square of the pressure coefficient is shown in Figure 27 for several Mach numbers. On the left is data from points at an elevation angle near  $45^\circ$  and on the right is data near  $21^\circ$ . For the higher transonic Mach numbers, there is a peak value at a viewing angle of  $90^\circ$ , where the unsteady shock is located. Similar  $C_{p,RMS}$  results were found during wind tunnel testing [23]. At the higher elevation points there is also an increase in the RMS near a viewing angle of  $70^\circ$ , which does not appear at lower elevation angle. In the full paper this will be looked into with more detail, but it is believed that it is likely due to the small trunnion gaps on the hemisphere surface. The higher elevation points correspond to data sets where the turret azimuthal angle is near  $90^\circ$  and the gaps are perpendicular to the flow, whereas the lower elevation angle data corresponds to sets where the gaps are parallel to the flow.

The pressure spectra at  $\alpha = 90^\circ$ , depicted in Figure 28, have peaks around  $St = 0.15$  for all Mach numbers. The amount of energy at the peak Strouhal number increases as Mach number increases, particularly between Mach  $0.7$  and  $0.8$ . This has been shown in previous studies to be the Strouhal number for the separation line motion [22] and for the unsteady shock at high transonic Mach numbers [20].

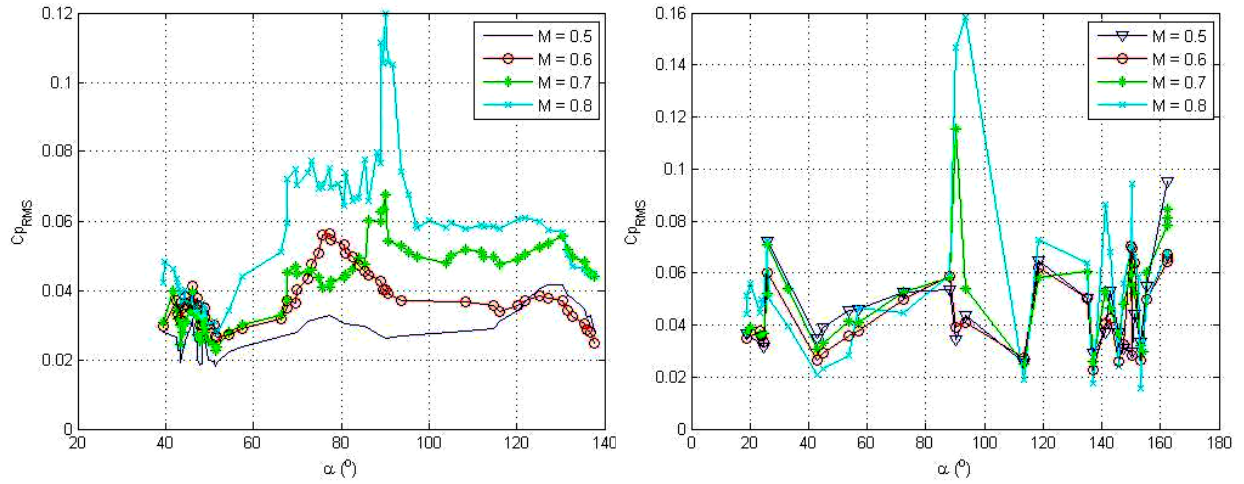


**Figure 27.  $C_{p,RMS}$  vs viewing angle on the hemisphere for varying Mach number with  $El = 45^\circ$ , left, and  $El = 21^\circ$ , right.**

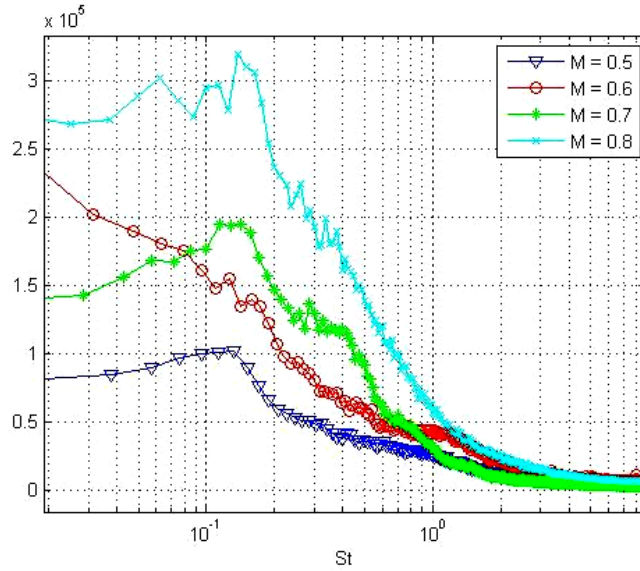


**Figure 28. Pressure spectra for varying Mach number at  $\alpha = 90^\circ$ .**

Figure 29 shows the mean removed spatial-temporal pressure field near a viewing angle of 90 degrees at a Mach number of 0.8. There are peaks and troughs near the viewing angle  $90^\circ$  due to the shock motion. The pressure fluctuations do not appear to be pure periodic, and have a time scale similar to that of the optical shock motion measured for a hemisphere-on-cylinder configuration at the same Mach number [20].



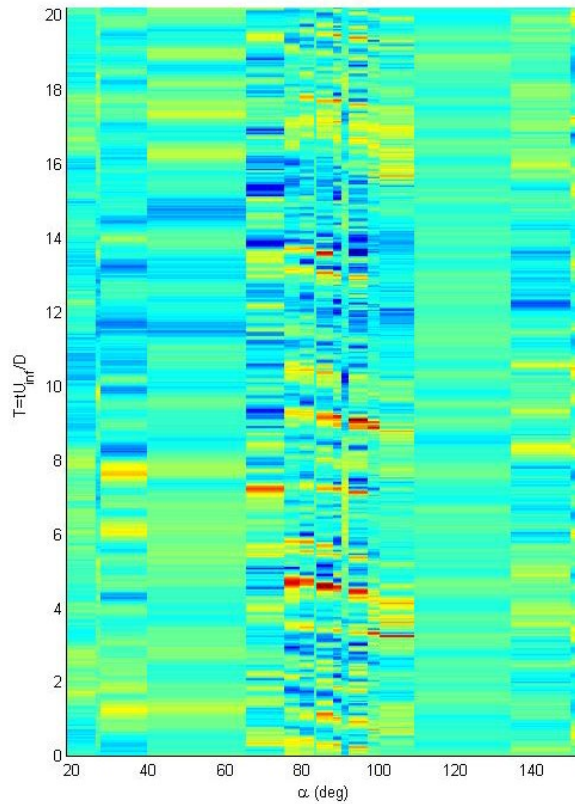


Figure 29. Mean removed spatial-temporal pressure field for  $M = 0.8$ .

## V. HIGH-FIDELITY COMPUTATIONS OF AERO-OPTICS

**Aero-Optics of 3-D Turrets.** Large-eddy simulations (LES) of hemisphere-on-cylinder turrets have continued over the past year with a focus on the effects of realistic turret geometric features and realistic Reynolds numbers on the flow and aero-optics. The simulations are performed using an unstructured-mesh LES code, Charles, developed by Cascade Technologies, Inc. [26]. A wall model was employed to reduce the severe near-wall grid resolution requirement and make the simulations more affordable.

A baseline simulation for the canonical smooth hemisphere-on-cylinder turret in Mach 0.4 flow at a reduced Reynolds number of  $4.6 \times 10^5$  (approximately 1/5 of the flight value) was previously examined [27]. It showed that the LES under-predicted the magnitude of the normalized  $OPD_{rms}$  when compared to AAOL experimental measurements at off-centerline viewing angles. To investigate the cause of this discrepancy, realistic geometric features like the gaps and ‘smiles’ that exist in the AAOL turret have been introduced into simulations.

In the past year the flow over a conformal turret with trunnion gaps aligned with flow direction was simulated at the reduced Reynolds number using approximately 61 million computational cells [28]. From the calculation, it was shown that the pressure difference on the turret surface drives flow from the front of the turret and redirects it to the top through the gaps (see Figure 30). This jetting effect causes an increase in density fluctuations near the aperture region as the jetted flow is convected into the turbulent wake. This leads to an increase in  $OPD_{rms}$  across all backward-viewing angles with larger differences seen at higher elevation angles as shown in Figure 31. The presence of the trunnion gaps also alters the spatial characteristics of the wavefronts in the Proper Orthogonal Decomposition (POD) modes presented in Figure 32. As POD decomposes data into modes ranked in terms of “energy” content, regions of the aperture affected by the gaps become

more important when they are compared with the baseline case. These results imply that in the development of adaptive-optic methods using similar data decompositions, the effect of viewing-angle dependent turret surface features (like gaps) may need to be taken into account as they can change the spatial structures of wavefronts.

Along with aero-optics, the effect of the gaps on the wake dynamics and the unsteady pressure on the surface of the turret are being investigated. Turrets with different gap orientations relative to the flow are also being simulated to find the effect of gaps in other configurations where the jetting may be less prevalent but can cause other flow separation and boundary layer effects.

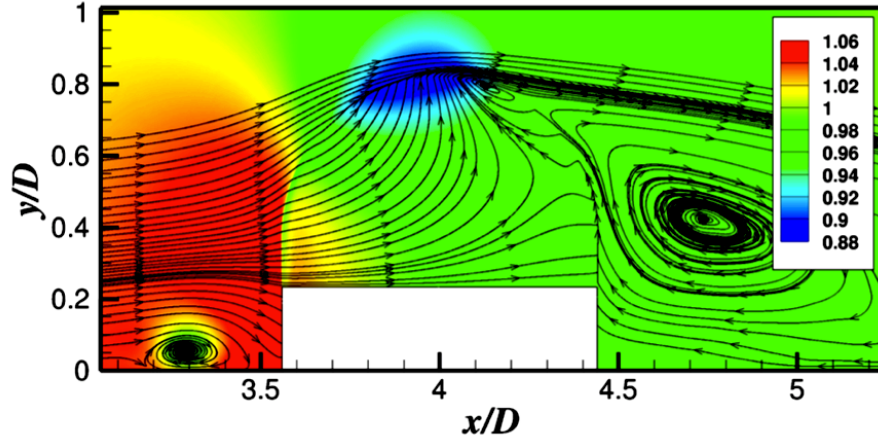


Figure 30. Streamlines of the time-averaged velocity in the mid-plane of the gap at  $z = 0.236D$  showing the flow path through the turret gaps. Colored contours are of  $p/p_\infty$ .

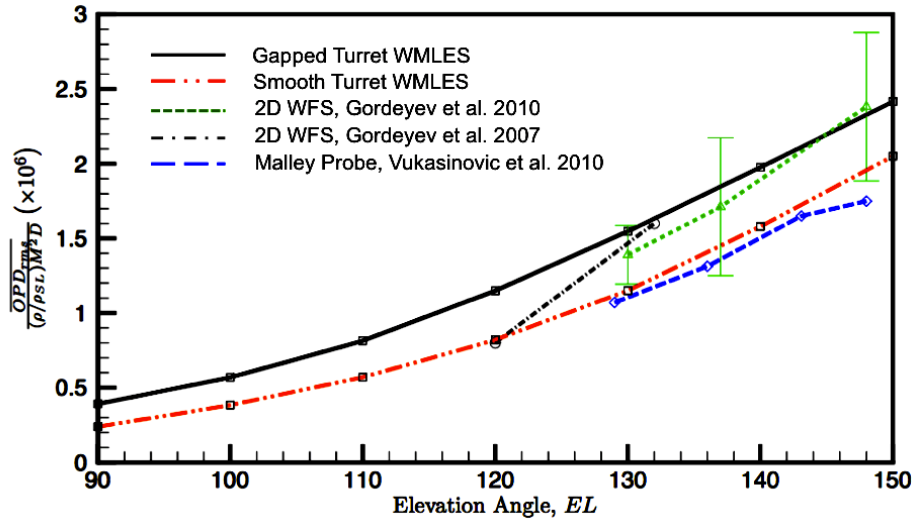
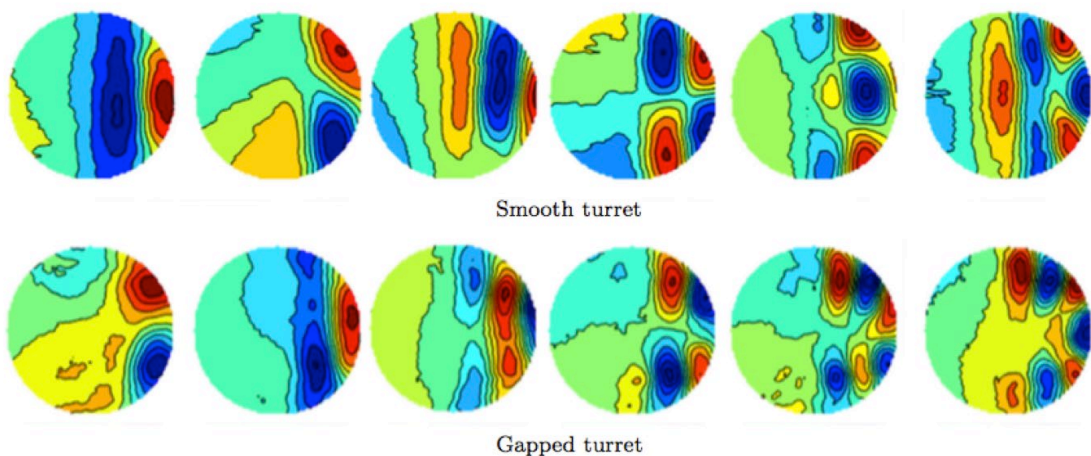
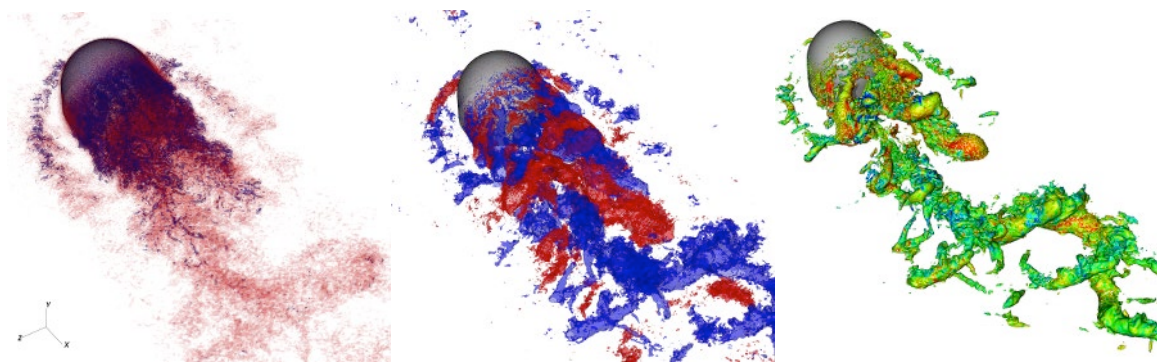


Figure 31. Normalized mean  $OPD_{rms}$  in the turret wake: Simulation values with and without gaps present.



**Figure 32. First six POD modes of smooth and gapped turret at an elevation angle of 120°. POD mode rank is descending from left to right.**

The 3-D turret simulations are computationally very expensive, and efforts have been made to acquire external computational resources to support AAOL-T computations. Edwin Mathews, the graduate students who carried out the 3-D turret simulations, was awarded a prestigious Blue Waters graduate fellowship from the National Science Foundation, which provided two million core hours on the Blue Waters Supercomputing facility in FY 2014-15. A comparable allocation has been awarded for FY 2015-16. Using these resources a comprehensive study of the smooth conformal turret at the full Reynolds number of  $2.3 \times 10^6$  was performed. The highly refined mesh contains over 200 million computational cells and this simulation is the largest numerical computation of a hemisphere-on-cylinder turret to date, providing unprecedented insight into the canonical turret flow. Visualizations of vortex structures, fluctuating density, and fluctuating pressure that show the complexity of the turret wake are displayed in Figure 33.



**Figure 33. Visualizations of lambda 2 (vortex identification method), fluctuating density, and fluctuating pressure in the turret wake from the full Reynolds number simulation.**

Utilizing the I/O capabilities of Blue Waters and data mining techniques, the aero-optics and fluid mechanics over the entire turret field of regard will be thoroughly investigated. The simulation generated a database of over 100 Terabytes of flow and optical data that will be used to gain key insights into the link between global flow phenomena and optical distortions. Simulation results for the pressure coefficient and optical distortion magnitude compare well with experimental measurements, as shown in Figure 34, and will be used in the near future to compare with results from the AAOL.

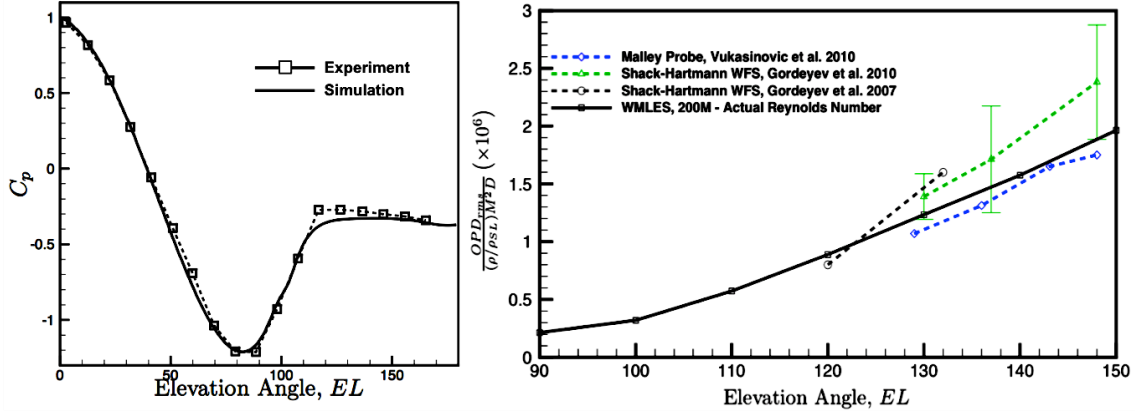


**Figure 34. Pressure coefficient and normalized OPD<sub>rms</sub> along the centerline of the turret compared with experimental measurements.**

**Turbulent Boundary Layers.** To evaluate the accuracy of wall-modeled LES for aerodynamic predictions and extend this method to transonic and supersonic flows, canonical configurations including subsonic and supersonic boundary layers and a 2-D cylindrical turret have been considered. The turbulent boundary layers are simulated at subsonic and supersonic speeds over a wide range of high Reynolds numbers. The simulation set-up is depicted schematically in Figure 35. The computational domain size is  $45\delta \times 15\delta \times 3.1\delta$ , where  $\delta$  is the boundary layer thickness at the aperture center. With grid resolutions of  $\Delta x = 0.05\delta$ ,  $\Delta z = 0.032\delta$  and  $\Delta y_{min} = 0.01\delta$  in streamwise, spanwise and wall-normal directions, respectively, the computational mesh contains 9 million cells.

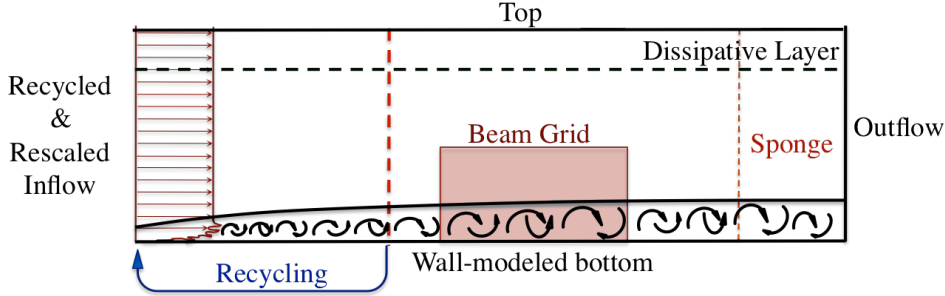


**Figure 35. Schematic of the computational set-up for turbulent boundary layers.**

Subsonic boundary layers are simulated at  $M_\infty = 0.5$  and a range of momentum-thickness Reynolds numbers  $Re_\theta$  from 2800 to 31000. In comparison with the wall-resolved LES of Wang and Wang [29] at  $Re_\theta = 3550$ , the computational expenses are reduced by two orders of magnitudes due to the application of a wall model. The basic flow statistics are shown in Figure 36. The mean velocity profiles show good agreement with the logarithmic law. The root-mean-square (rms) values of the streamwise velocity fluctuations are also in reasonable agreement with the experimental measurements of DeGraaff and Eaton [30] at  $Re_\theta = 2900, 5200, 13000$  and 31000, which are the closest matches to the Reynolds numbers in the simulations.



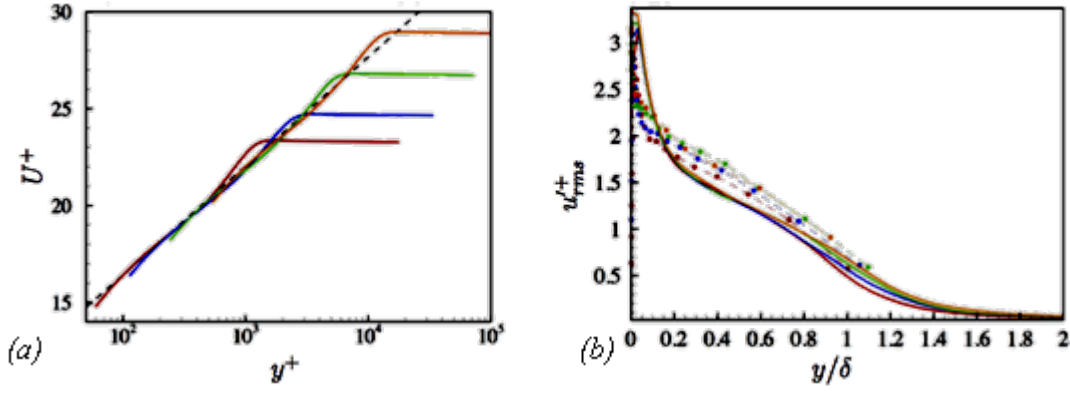


**Figure 36. Streamwise velocity statistics in Mach 0.5 turbulent boundary layers: (a) Mean velocity profiles; (b) rms of streamwise velocity fluctuations. Wall-modeled LES: —,  $Re_\theta = 2800$ ; —,  $Re_\theta = 5600$ ; —,  $Re_\theta = 13000$ ; —,  $Re_\theta = 31000$ . Experimental measurements of DeGraaff and Eaton [5]: - - - ,  $Re_\theta = 2900$ ; - - - ,  $Re_\theta = 5200$ ; - - - ,  $Re_\theta = 13000$ ; - - - ,  $Re_\theta = 31000$ . - - - , logarithmic law.**

Simulations of supersonic boundary layers are conducted at  $M_\infty = 1.7, 2.0$  and  $3.0$ , with  $Re_\theta = 5.0 \times 10^4, 6.9 \times 10^4$ , and  $5.0 \times 10^4$ , respectively. The first case matches the experimental parameters of Souverein et al. [31] whereas the last two cases correspond to the experimental conditions of Gordeyev et al. [32, 33]. As shown in Figure 37, the predicted Van Driest transformed mean velocity profiles match the logarithmic law very well, and the rms values of streamwise velocity fluctuations at  $M = 1.7$  and  $Re_\theta = 5.0 \times 10^4$  show a reasonable agreement with the experimental data of Souverein et al. [31].

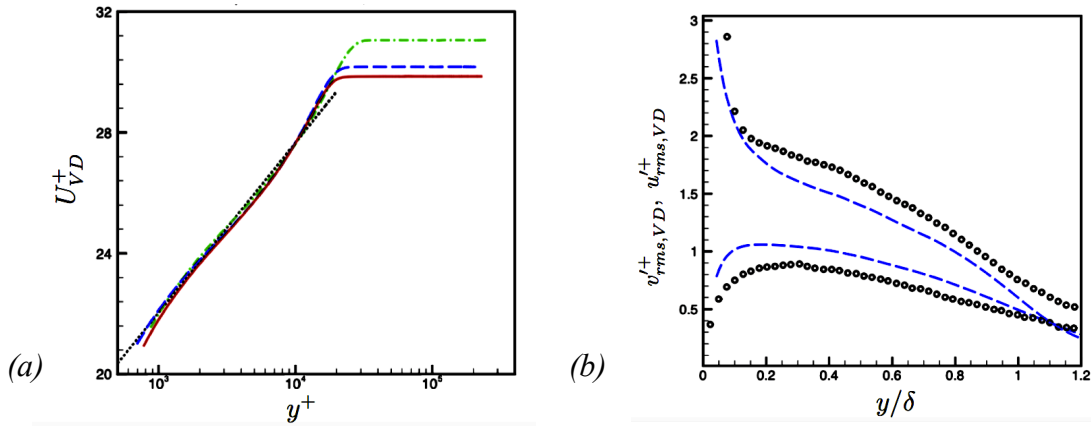


**Figure 37. Van Driest transformed velocity statistics: (a) Mean streamwise velocity; (b) rms of streamwise and wall-normal velocity fluctuations. — — — ,  $M_\infty = 1.7, Re_\theta = 5.0 \times 10^4$ ; - . - . - ,  $M_\infty = 2.0, Re_\theta = 6.9 \times 10^4$ ; — ,  $M_\infty = 3.0, Re_\theta = 5.0 \times 10^4$ ;  $\circ$ , experimental measurement of Souverein et al. at  $M_\infty = 1.7$  and  $Re_\theta = 5.0 \times 10^4$ ; - - - - - , logarithmic law.**

Figure 38 compares the normalized  $OPD_{rms}$  at free-stream Mach numbers  $M_\infty = 0.5, 2.0$  and  $3.0$  with experimental measurements and the prediction by a model (ND model) developed by Gordeyev et al. [33]. The wall-modeled LES results show the correct trend and reasonable

agreement with experimental data at these three Mach numbers, but the rate of change with Mach number deviates from the experimental measurements. The sources of the discrepancy are currently under investigation.

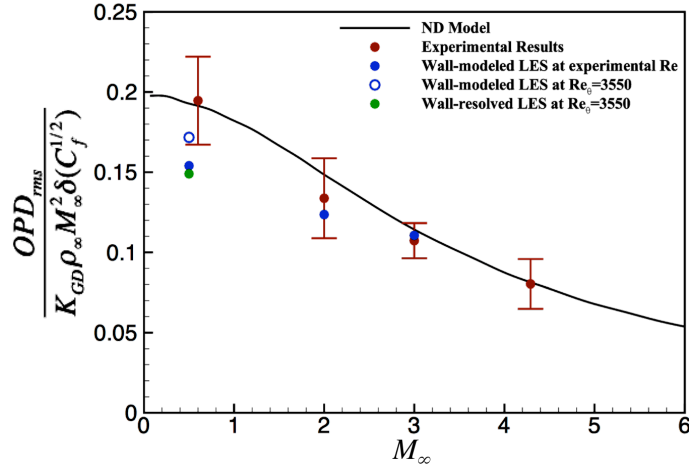


Figure 38. Normalized aero-optical distortion magnitude for turbulent boundary layers.

**Subsonic Flow over a Cylindrical Turret with a Flat Window.** The flow over a cylindrical turret with a flat window has been simulated under the same conditions as in the experiment of Gordeyev et al. [34]:  $M = 0.5$  and  $Re_R = 5.6 \times 10^5$  based on the turret radius  $R$ . As shown schematically in Figure 39, the computational inlet is located  $2.75R$  upstream of the turret axle, and the elevation angle of the turret is fixed at  $120^\circ$ . The inflow turbulence data are generated by a separate flat-plate boundary layers simulation. The inlet boundary-layer thickness  $\delta_{in}$  is approximately  $0.14R$  and the momentum-thickness Reynolds number is  $Re_{\theta} = 7650$ . The domain size is  $12.6R \times 2.81R \times 0.422R$ . This wall-modeled LES at the *full* experimental Reynolds number employs a mesh with only 4.9 million grid cells. The computational expense is approximately 10% of that of the wall-resolved LES by Wang et al. [35], which was performed at 16% of the experimental Reynolds number. The computed velocity and density statistics at four streamwise locations above the optical window are compared to the experimental measurements and wall-resolved LES results. As can be seen in Figures 40 and 41, reasonable agreement is obtained.

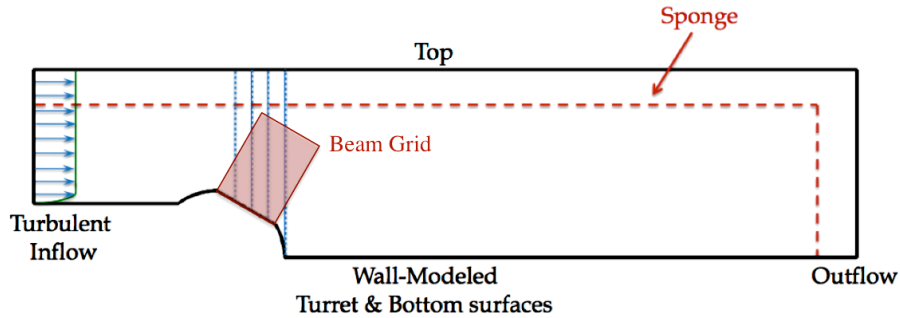


Figure 39. Schematic of the computational set-up for subsonic flow over a cylindrical turret with a flat window. Dashed blue lines are the locations where comparisons are made with the experimental data and previous simulation results.

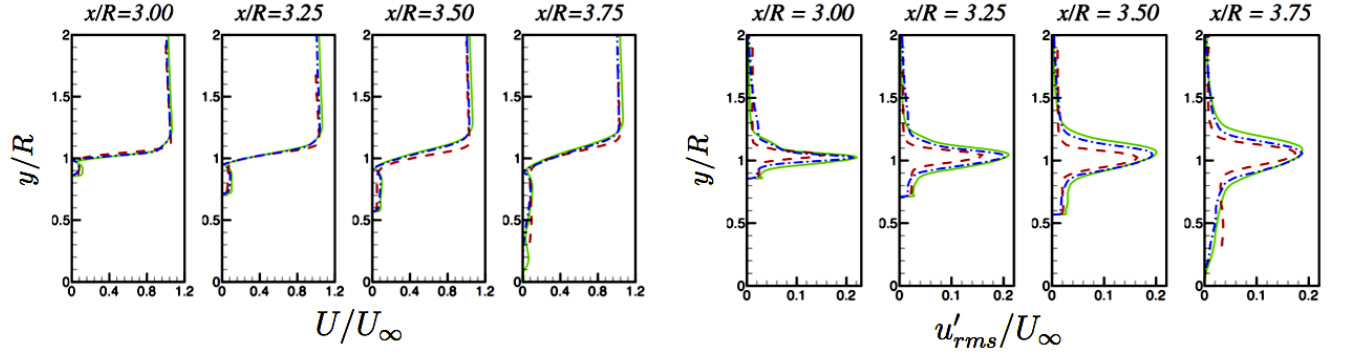


Figure 40. (a) Mean streamwise velocity profiles and (b) rms of velocity fluctuations at four locations above the optical window: —, wall-modeled LES; ---, wall-resolved LES of Wang et al. [10] at a reduced Reynolds number; -.-, experiment of Gordeyev et al. [35].

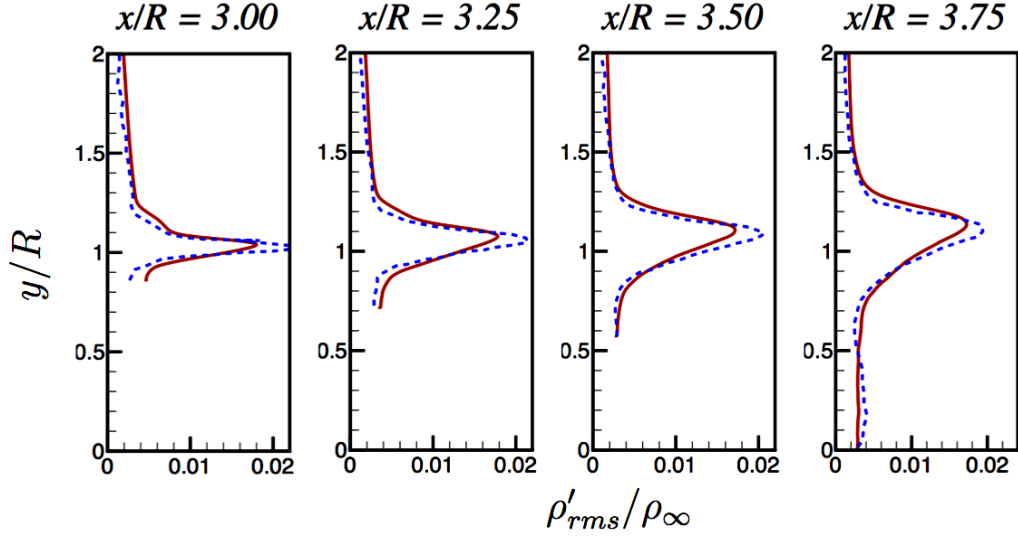
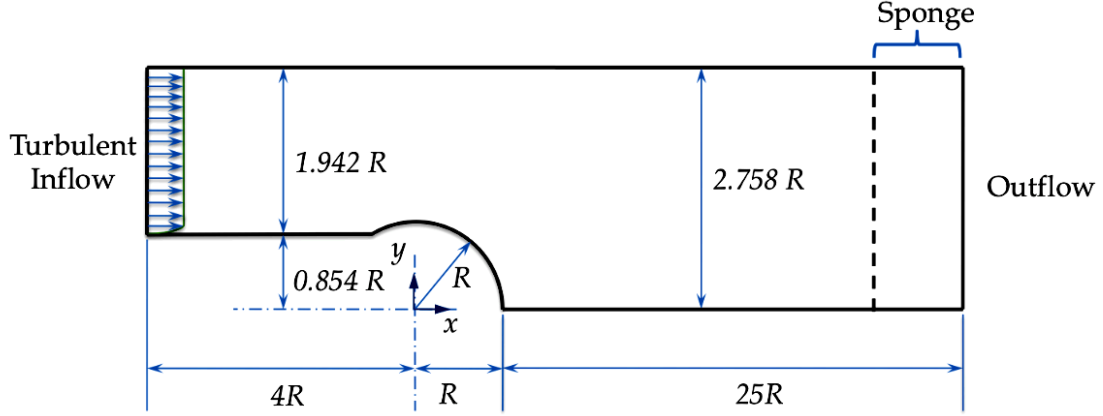


Figure 41. Density fluctuations above the optical window: —, wall-modeled LES; ---, wall-resolved LES at a reduced Reynolds number.

An aperture size of  $1.0R \times 0.422R$  is employed for optical calculation. The time-averaged  $OPD_{rms}$  from the wall-modeled LES is  $7.17 \times 10^{-7}R$ , which agrees well with the value of  $7.10 \times 10^{-7}R$  from the wall-resolved LES and is approximately 10% higher than the experimentally measured value of  $6.39 \times 10^{-7}R$ .

**Transonic Flow over a Cylindrical Turret with a Conformal Window.** The experiment of Vorobiev et al. [5] is being simulated by using wall-modeled LES. The computational set-up in the  $x$ - $y$  plane is illustrated in Figure 42. Time-dependent turbulent inflow at  $M_{in} = 0.68$  and  $Re_{\theta,in} = 10^4$ , which match the experimental parameters, is fed into the simulation domain, and the back pressure in the simulation is determined iteratively to match the experimental mean pressure measured in the wind tunnel. The current mesh consists of 15 million cells. In Figure 43, the numerical schlieren is displayed along with shadowgraphs from the experiment. These preliminary results show qualitative agreement with experimental observations in terms of different patterns of shock/wake dynamics as the back pressure is decreased from 98% to 77% of the inlet static pressure. The

simulations are ongoing and will be validated against experimental measurements, and optical distortions and their relation to the shock dynamics will be investigated.



**Figure 42. Schematic of the computational set-up for transonic flow over a cylindrical turret with a conformal window. Dimensions are presented in terms of turret radius  $R$ .**

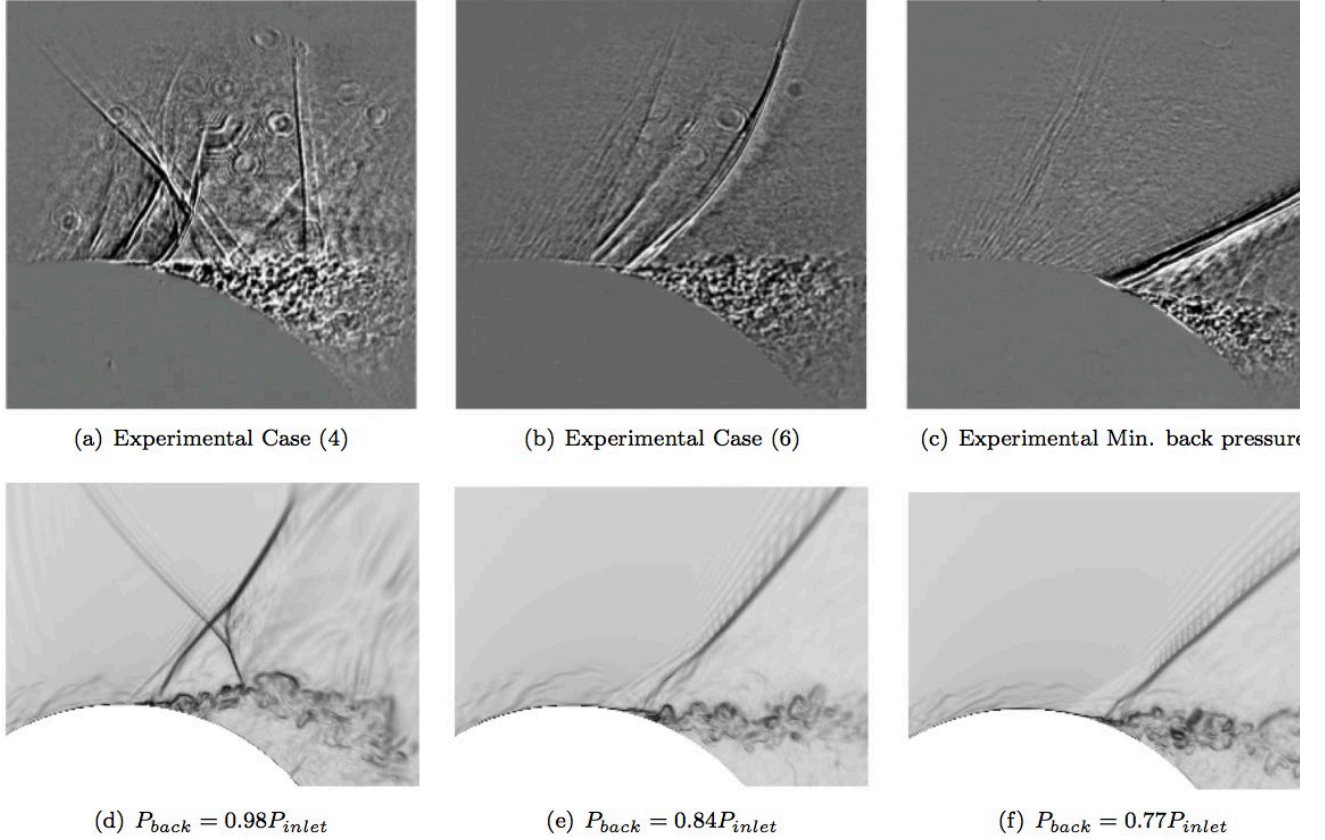


**Figure 43. A qualitative comparison between the shadowgraphs (a, b and c) of the experiment conducted by Vorobiev et al. [11] and the numerical schlieren ( $NS=0.8\exp[10(|\nabla\phi|-|\nabla\phi|_{\min})/(|\nabla\phi|_{\max}-|\nabla\phi|_{\min})]$ ) of the current simulations at different back pressures (d, e and f).**

## VI. ADVANCES IN PREDICTIVE AERO-OPTIC CONTROL

A challenge to the implementation of real-time adaptive optic systems on aircraft is the latency problem [36]. Frequencies associated with dominant aero-optic aberrations are typically on the order of hundreds or thousands of kilohertz for practical applications. Small delays in an adaptive-optic feedback controller can cause substantial performance degradation or even instability. The source of this delay is the cumulative latency in digital processing; input/output communication between deformable mirrors, sensors, and processors; and dead-time in mechanical system response. Dead-time is conventionally viewed as a difficult problem to deal with in feedback control [37]: regardless of the quality of a controller, the controller fundamentally cannot respond to a sensed disturbance for at least the duration of the cumulative dead time. The effect of this is to put an upper limit on controller performance and bandwidth.

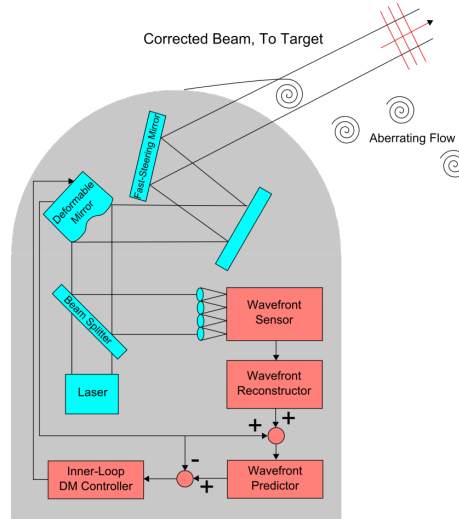


Figure 44. Feedforward system architecture [36]

One method for overcoming this obstacle is to use a *feedforward* predictor in conjunction with a feedback controller. This feedforward element uses prior knowledge of disturbance dynamics to predict the evolution of an aberrating flow over a short temporal horizon, equal to the cumulative feedback controller delay. The improved control architecture is shown in Figure 44. Since aero-optic applications typically involve hundreds of subapertures, it is desirable to reduce the dimensionality of the prediction problem. A method was investigated this year that relies on model reduction using Proper Orthogonal Decomposition [38] and a neural network [39] to predict the temporal evolution of the POD coefficients.

To analyze performance of this proposed system, we divided the flow into three general regions depending on viewing angle,  $\alpha$ . For  $\alpha < 90$  deg., the flow is fully attached and the resulting aero-optical aberrations are not severe. Between 90 and 120 degrees we begin to witness the onset of separation, and the optical aberrations begin to become larger. At viewing angles of 120 degrees and larger, the flow becomes fully separated and the aero-optical aberrations become very large. Fortunately, we have discovered that the fully separated flow has more predictable behavior that approximates a shear layer: that is, the most optically-active region is also the easiest to predict. This means that a predictive controller will actually perform better for the flow region with the worst aberrations, which is a favorable characteristic. We simulated a closed-loop adaptive-optic control system operating at 25 kHz (equivalent to the wavefront sensor sample rate of the flight test data). In the separated region, we achieved approximately -3.5dB (about 55%) wavefront

disturbance rejection for small amounts (1 timestep, or  $40 \mu\text{s}$ ) of latency, and about -2dB (about 35%) wavefront disturbance rejection for larger amounts (5 timesteps, or  $200 \mu\text{s}$ ) of latency.

Since this paper was published early this year, we have developed an updated prediction model that is computationally less intensive as well as more robust and accurate. Like the neural network model, it relies on prior knowledge of flow behavior to make predictions; however, it is purely linear and thus its stability characteristics may be more easily understood.

We may decompose each wavefront at timestep  $k$ ,  $\mathbf{v}_k$ , into a summation of POD modes,  $\Phi_n$ , multiplied by corresponding temporal coefficients  $x_k$ , as follows,

$$\mathbf{v}_k = \sum_{n=1}^N x_n(k) \Phi_n.$$

To perfectly reconstruct a wavefront, the POD modes must span the entire set if the training matrix is full rank. In general, this will be true for experimental data, although the highest-order modes are likely contaminated with noise. Thus, the value for  $N$  will be equal to the number of subapertures in the wavefront matrix for a perfect reconstruction. In practice, it is desirable to truncate the set of modes used for reconstruction to reduce noise and reduce computational requirements for the prediction model. In general, the low-order POD modes will capture the motion of coherent turbulent structures across the optical aperture.

The goal for the coefficient prediction function,  $\mathbf{g}$ , is to estimate future POD coefficients based on the past  $M$  measurements while minimizing the norm of the prediction residual error,  $\epsilon_{k+1}$ ,

$$\mathbf{v}_{k+1} = \Phi_1^N \mathbf{g}(\mathbf{x}_k, \mathbf{x}_{k-1}, \dots, \mathbf{x}_{k-M+1}) + \epsilon_{k+1}.$$

The coefficient prediction is then multiplied by the POD modes to obtain the full wavefront prediction,  $\mathbf{v}_{k+1}$ . For multi-step prediction, this function is used recursively.

We found a practical prediction limit of about 16 POD modes using the POD/neural network method. Beyond this number of modes, the improvement in prediction accuracy diminished so rapidly that the extra computational requirements were not really justifiable. With the more stable and accurate linear predictor, we have observed consistently better performance up to about 64 modes.

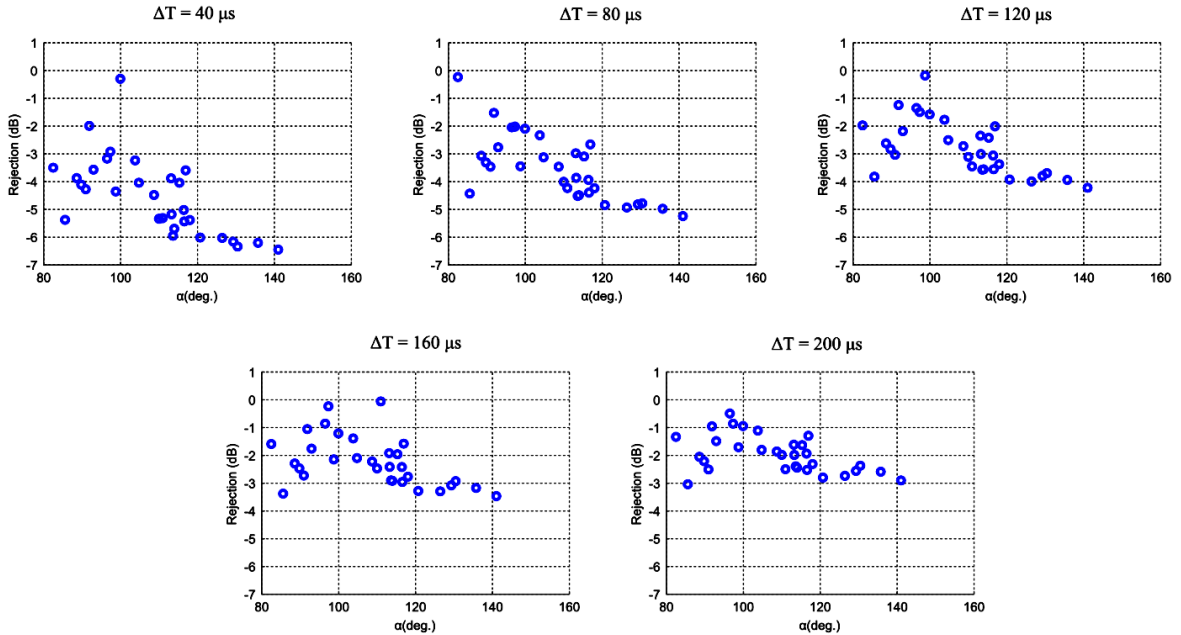


**Figure 45: Simulated mean disturbance rejection using flight test data for varying amounts of latency, assuming a 25kHz control loop**



The resulting error rejection functions are shown in Figure 45 for varying amounts of latency. Up to -6.5 dB (or 78%, compared to -3.5 dB or 55% previously) of error rejection are seen for small amounts of latency. For larger amounts of latency, we observe up to -3dB (or 50%, compared to -2dB or 35%) of rejection.

Future work will focus on improving the quality of the predictions, as well as methods to improve the robustness of the method as the flow condition slowly changes as a function of Mach number, altitude, viewing angle, etc. These improvements are important, because system performance approximately degrades with RMS wavefront error *squared*. This is illustrated in Figure 46. For example, a -3dB wavefront error reduction corresponds to a taking an uncorrected Strehl Ratio of 0.2 to 0.67.

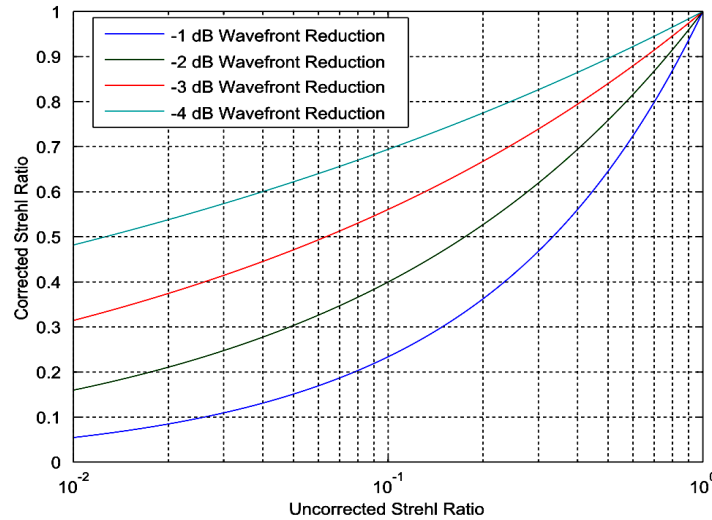


**Figure 46: Corrected and uncorrected Strehl ratios as a function of mean wavefront error reduction**

## VII. CONCLUDING REMARKS

Please keep in mind that this report reflects only the highlights of what we accomplished in the third year of this grant; not included is, for example, the efforts undertaken to support the DARPA/AFRL 40% ABC turret except for a short mention that we are doing this. The work on adaptive optics was only touched on; since this work is still very much in progress, I intend to give a more detailed report on this area in next year's report. Even so, it is clear that the grant has been extremely productive.

This effort has at least partially supported 5 faculty, 1 research specialist, 2 post-doctoral fellows, 1 research staff, and 10 graduate students.

## REFERENCES

- [1] E Jumper, M Zenk, S Gordeyev, D Cavalieri and M. Whiteley, "Airborne Aero-Optics Laboratory", *Journal of Optical Engineering*, **52**(7), 071408, 2013.
- [2] C. Porter, S. Gordeyev, M. Zenk and E. Jumper, "Flight Measurements of the Aero-Optical Environment around a Flat-Windowed Turret", *AIAA Journal*, Vol. 51, No. 6, Jun. 2013, pp. 1394-1403.
- [3] N. De Lucca, S. Gordeyev and E.J. Jumper, "In-flight aero-optics of turrets", *Journal of Optical Engineering*, **52**(7), 071405, 2013.

- [4] R. Burns, S. Gordeyev, E. Jumper, S. Gogineni, M. Paul and D.J. Wittich, "Estimation of Aero-Optical Wavefronts Using Optical and Non-Optical Measurements ", AIAA Paper 2014-0319, 2014.
- [5] A. Vorobiev, S. Gordeyev, E. Jumper, S. Gogineni, A. Marruffo and D.J. Wittich, "Low-Dimensional Dynamics and Modeling of Shock-Separation Interaction over Turrets at Transonic Speeds", AIAA Paper 2014-2357, 2014.
- [6] S. Gordeyev and E. Jumper, "Fluid Dynamics and Aero-Optics of Turrets", *Progress in Aerospace Sciences*, **46**, (2010), pp. 388-400.
- [7] N. De Lucca, S. Gordeyev, E. Jumper and D.J. Wittich, "Aero-Optical Environment around Turrets at Forward-Viewing Angles", AIAA Paper 2013-0721, 2013.
- [8] R. Jelic, S. Sherer and R. Greendyke, "Simulation of Various Turret Configurations at Subsonic and Transonic Flight Conditions Using OVERFLOW", *Journal of Aircraft*, **50**, pp. 398-409, 2013.
- [9] Courier, W.J., Whiteley, M., Goorskey, D.J., Drye, R., Barber, J., Stutts, J. and Porter, C., "Aero-Optical Evaluation of Notional Turrets in Subsonic, Transonic and Supersonic Regimes", AIAA Paper 2014-2355, 2014.
- [10] Jumper, E.J., Gordeyev, S., Cavalieri, D. and Rollins, P. "Airborne Aero-Optics Laboratory - Transonic (AAOL-T)," AIAA Paper 2015-0675, 2015.
- [11] S. Gordeyev, N. De Lucca, E. Jumper, K. Hird, T.J. Juliano, J.W. Gregory, J. Thordahl and D.J. Wittich, "Comparison of Unsteady Pressure Fields on Turrets with Different Surface Features using Pressure Sensitive Paint ", *Experiments in Fluids*, **55**, p. 1661, 2014.
- [12] N. De Lucca, S. Gordeyev and E.J. Jumper, "Global Unsteady Pressure Fields Over Turrets In-Flight", AIAA Paper 2015-0677, 2015.
- [13] Goorskey, D.J., Drye, R. and Whiteley M.R., "Dynamic modal analysis of transonic Airborne Aero-Optics Laboratory conformal window flight-test aero-optics," *Opt. Eng.* **52** (7), 071414, 2013.
- [14] M. Wang, A. Mani and S. Gordeyev, "Physics and Computation of Aero-Optics", *Annual Review of Fluid Mechanics*, **44**, pp. 299-321, 2012.
- [15] B. Vukasinovic, A. Glezer, S. Gordeyev, E. Jumper and V. Kibens, "Hybrid Control of a Turret Wake," *AIAA Journal*, **49**(6), pp. 1240-1255, 2011.
- [16] M. Palavicchini, L. Cattafesta and B. George, "Passive Flow Control over a Three-Dimensional Turret with a Flat Aperture", AIAA Paper 2011-3265, 2011.
- [17] D.S. Dolling, "Fifty years of shock-wave/boundary-layer interaction research: what next?", *AIAA Journal*, **39**(8), pp. 1517-1531, 2001.
- [18] Green J.E. "Interaction between shock waves and boundary layers" *Progress in Aerospace Sciences*, **11**, pp. 235-340, 1970.
- [19] Delery J.M. "Shock wave/turbulent boundary layer interaction and control", *Prog. Aerospace Sci.*, **22**, pp. 209-280, 1985.
- [20] J. Morrida, S. Gordeyev, N. De Lucca, E. Jumper. "Aero-Optical Investigation of Transonic Flow Features and Shock Dynamics on Hemisphere-On-Cylinder Turrets", AIAA Paper 2015-0676, 2015.
- [21] E.J. Jumper, S. Gordeyev, D. Cavalieri, P. Rollins, M.R. Whiteley and M.J. Krizo, "Airborne Aero-Optics Laboratory - Transonic (AAOL-T)," AIAA Paper 2015-0675, 2015.
- [22] S. Gordeyev, N. De Lucca, E. Jumper, K. Hird, T.J. Juliano, J.W. Gregory, J. Thordahl and D.J. Wittich, "Comparison of Unsteady Pressure Fields on Turrets with Different Surface Features using Pressure Sensitive Paint ", *Experiments in Fluids*, **55**, p. 1661, 2014.
- [23] J. Morrida, S. Gordeyev, E. Jumper, "Investigation of Shock Dynamics on a Hemisphere Using Pressure and Optical Measurements", submitted to AIAA SciTech Conference, 2016.

- [24] Courier, W.J, Porter, C., Barber, J., Stutts, J., Whiteley, M., Goorskey, D. and Drye, R., "Aero-Optical Evaluation of Notional Turrets in Subsonic, Transonic and Supersonic Regimes," AIAA Paper 2014-2355, 2014.
- [25] R. Jelic, S. Sherer and R.Greendyke, "Simulation of Various Turret Configurations at Subsonic and Transonic Flight Conditions Using OVERFLOW", *Journal of Aircraft*, **50**, pp. 398-409, 2013.
- [26] Khalighi, Y., Nichols, J.W., Ham, F., Lele, S.K. and Moin, P., "Unstructured Large Eddy Simulation for Prediction of Noise Issued from Turbulent Jets in Various Configurations". AIAA Paper 2011-2886.
- [27] Mathews, E., Wang, K., Wang, M. and Jumper, E., "LES Analysis of Hemisphere-on-Cylinder Turret Aero-Optics". AIAA Paper 2014-0323.
- [28] Mathews, E., Wang, K., Wang, M., and Jumper, E., "Numerical Investigation of Aero-Optical Distortions over a Hemisphere-on-Cylinder Turret with Gaps". AIAA Paper 2015-3248.
- [29] Wang, K. and Wang, M., "Aero-Optics of Subsonic Turbulent Boundary Layers," *Journal of Fluid Mechanics*, Vol. 696, 2012, pp. 122–151.
- [30] DeGraaff, D. B. and Eaton, J. K., "Reynolds-Number Scaling of the Flat-Plate Turbulent Boundary Layer," *Journal of Fluid Mechanics*, Vol. 422, 2000, pp. 319–346.
- [31] Souverein, L. J., Dupont, P., Debiève, J.-F., Van Oudheusden, B. W., and Scarano, F., "Effect of Interaction Strength on Unsteadiness in Shock-Wave-Induced Separations," *AIAA journal*, Vol. 48, No. 7, 2010, pp. 1480–1493.
- [32] Gordeyev, S., Jumper, E., and Hayden, T. E., "Aero-Optical Effects of Supersonic Boundary Layers," *AIAA journal*, Vol. 50, No. 3, 2012, pp. 682–690.
- [33] Gordeyev, S., Rennie, R. M., Cain, A. B., and Hayden, T. E., "Aero-Optical Measurements of High-Mach Supersonic Boundary Layers," AIAA Paper 2015-3246.
- [34] Gordeyev, S., Cress, J., Smith, A., and Jumper, E. J., "Improvement in Optical Environment over Turrets with Flat Window Using Passive Flow Control," AIAA Paper 2010-4492.
- [35] Wang, K., Wang, M., Gordeyev, S., and Jumper, E., "Computation of Aero-Optical Distortions over a Cylindrical Turret with Passive Flow Control," AIAA paper 2010-4498.
- [36] R. Burns, E. Jumper, and S. Gordeyev, "A Latency-Tolerant Architecture for Airborne Adaptive Optic Systems," *53rd Aerosp. Sci. Meet.*, 2015.
- [37] V. VanDoren, "Overcoming the deadtime dilemma," *Control Engineering*, vol. 44, no. 8, p. 120, Jun-1997.
- [38] G. Berkooz, P. Holmes, and J. L. Lumley, "The Proper Orthogonal Decomposition in the Analysis of Turbulent Flows," *Annu. Rev. Fluid Mech.*, vol. 25, no. 1, pp. 539–575, 1993.
- [39] K. Hornik, M. Stinchcombe, and H. White, "Multilayer Feedforward Networks Are Universal Approximators," *Neural Netw.*, vol. 2, no. 5, pp. 359–366, 1989.

REPORT DOCUMENTATION PAGE				Form Approved OMB No. 0704-0188	
<p>The public reporting burden for this collection of information is estimated to average 1 hour per response, including the time for reviewing instructions, searching existing data sources, gathering and maintaining the data needed, and completing and reviewing the collection of information. Send comments regarding this burden estimate or any other aspect of this collection of information, including suggestions for reducing the burden, to the Department of Defense, Executive Service Directorate (0704-0188). Respondents should be aware that notwithstanding any other provision of law, no person shall be subject to any penalty for failing to comply with a collection of information if it does not display a currently valid OMB control number.</p> <p><b>PLEASE DO NOT RETURN YOUR FORM TO THE ABOVE ORGANIZATION.</b></p>					
1. REPORT DATE (DD-MM-YYYY) 11-29-2018		2. REPORT TYPE Final Performance Report		3. DATES COVERED (From - To) Aug 2016-Aug 2018	
4. TITLE AND SUBTITLE Airborne Aero-Optics Laboratory-Transonic (AAOL-T)			5a. CONTRACT NUMBER N00014-16-1-3186		
			5b. GRANT NUMBER 12175346		
			5c. PROGRAM ELEMENT NUMBER		
6. AUTHOR(S) Dr. Eric J. Jumper			5d. PROJECT NUMBER		
			5e. TASK NUMBER		
			5f. WORK UNIT NUMBER		
7. PERFORMING ORGANIZATION NAME(S) AND ADDRESS(ES) DR. ERIC J. JUMPER UNIVERSITY OF NOTRE DAME 301 CUSHING HALL NOTRE DAME, IN 46556-5612				8. PERFORMING ORGANIZATION REPORT NUMBER	
9. SPONSORING/MONITORING AGENCY NAME(S) AND ADDRESS(ES) Dr. Sarwat Chappell Sea Platforms and Weapons Division 875 N. Randolph Arlington, VA 22203-1995				10. SPONSOR/MONITOR'S ACRONYM(S)	
				11. SPONSOR/MONITOR'S REPORT NUMBER(S)	
12. DISTRIBUTION/AVAILABILITY STATEMENT Unlimited, Approved for public release.					
13. SUPPLEMENTARY NOTES					
<b>14. ABSTRACT</b> <p>This report covers the fourth and fifth years of the Airborne Aero-Optics Laboratory-Transonic (AAOL-T) program. Aero-optics severely limits an airborne directed-energy system's lethal field of regard; aero-optics refers to the deleterious effect that the density fluctuations in the flow have on an airborne optical system. The AAOL-T program studies aero-optical aberration problems from experimental, theoretical and computational approaches; the most unique part of the program is that we also perform flight tests using Falcon 10's, capable of testing at greater than Mach 0.8. The program makes use of two aircraft, one to project a small-aperture, diverging beam toward an optical turret on the second, laboratory aircraft. The fourth and fifth years of the program have been productive with flights in support of both the baseline program and to support AFRL/DARPA 40% ABC Turret testing. During the baseline program, extensive measurements of aero-optical environment around both hemisphere-on-cylinder and hemisphere-only turrets were performed for Mach range between 0.5 and 0.8.</p>					
15. SUBJECT TERMS					
16. SECURITY CLASSIFICATION OF:			17. LIMITATION OF ABSTRACT  UU	18. NUMBER OF PAGES  53	19a. NAME OF RESPONSIBLE PERSON Mike Zenk
a. REPORT Unclassified	b. ABSTRACT Unclassified	c. THIS PAGE Unclassified			19b. TELEPHONE NUMBER (Include area code) 574-631-1189